Polymer Additive Manufacturing for Marine Renewable Energy Applications: Best Practices, Research Trends, and Current Challenges

Paul Murdy,[1] Charles Candon,[1] Daniel Samborsky,[2] David Miller,[2] and Ryan Beach[1]

1 National Renewable Energy Laboratory
2 Montana State University

NREL is a national laboratory of the U.S. Department of Energy
Office of Energy Efficiency & Renewable Energy
Operated by the Alliance for Sustainable Energy, LLC

This report is available at no cost from the National Renewable Energy Laboratory (NREL) at www.nrel.gov/publications.

Contract No. DE-AC36-08GO28308

Technical Report
NREL/TP-5700-90930
September 2024

Polymer Additive Manufacturing for Marine Renewable Energy Applications: Best Practices, Research Trends, and Current Challenges

Paul Murdy,[1] Charles Candon,[1] Daniel Samborsky,[2] David Miller,[2] and Ryan Beach[1]

1 National Renewable Energy Laboratory
2 Montana State University

Suggested Citation
Murdy, Paul, Charles Candon, Daniel Samborsky, David Miller, and Ryan Beach. 2024. *Polymer Additive Manufacturing for Marine Renewable Energy Applications: Best Practices, Research Trends, and Current Challenges*. Golden, CO: National Renewable Energy Laboratory. NREL/TP-5700-90930. https://www.nrel.gov/docs/fy24osti/90930.pdf.

NREL is a national laboratory of the U.S. Department of Energy
Office of Energy Efficiency & Renewable Energy
Operated by the Alliance for Sustainable Energy, LLC

This report is available at no cost from the National Renewable Energy Laboratory (NREL) at www.nrel.gov/publications.

Contract No. DE-AC36-08GO28308

Technical Report
NREL/TP-5700-90930
September 2024

National Renewable Energy Laboratory
15013 Denver West Parkway
Golden, CO 80401
303-275-3000 • www.nrel.gov

NOTICE

This work was authored in part by the National Renewable Energy Laboratory, operated by Alliance for Sustainable Energy, LLC, for the U.S. Department of Energy (DOE) under Contract No. DE-AC36-08GO28308. Funding provided by U.S. Department of Energy Office of Energy Efficiency and Renewable Energy Water Power Technologies Office. The views expressed herein do not necessarily represent the views of the DOE or the U.S. Government.

Cover Photos by Dennis Schroeder: (clockwise, left to right) NREL 51934, NREL 45897, NREL 42160, NREL 45891, NREL 48097, NREL 46526.

Acknowledgements

The authors would like to thank the affiliate laboratories and researchers that have helped make contributions to this research over the past 5 years as part of the Marine Energy Advanced Materials project, specifically those at Sandia National Laboratories, Pacific Northwest National Laboratory, Montana State University, and Florida Atlantic University. We would also like to acknowledge our technical monitors from the U.S. Department of Energy's Water Power Technologies Office—Lauren Ruedy, Carrie Noonan, and Collin Sheppard—for all of their guidance, support, and valuable feedback over the past 4 years. The authors thank the Colorado Office of Economic Development and International Trade (OEDIT) for funding some of the equipment in the Composite Manufacturing Education and Technology (CoMET) at NREL that was used for this research. Finally, this research would not have been possible without the valuable and diligent work performed by our research technicians who continue to support every aspect of this project—David Barnes, Sara Wallen, Victor Castillo, Bill Gage, Mike Jenks, and Joshua O'Dell.

List of Acronyms

AM	additive manufacturing
ANOVA	analysis of variance
ASA	acrylonitrile styrene acrylate
CNC	computer numerical control
DED	direct energy deposition
DEEC-Tec	distributed embedded energy converter technologies
FDM	fused deposition modeling
FRP	fiber-reinforced polymer
IPA	isopropyl alcohol
min	minute
mm	millimeter
MRE	marine renewable energy
NREL	National Renewable Energy Laboratory
RM3	Reference Model 3
SLA	stereolithography
SWEL	Sea Wave Environmental Laboratory
WPTO	Water Power Technologies Office

Executive Summary

Additive manufacturing (AM) is a rapidly growing technology space not only for prototyping but also at larger scales and with increasing component quantities. There are many AM processes and materials available to users, and effectively applying those processes and materials to a specific use case can be challenging. One specific area where AM could be particularly beneficial is marine renewable energy (MRE). Not only is MRE a relatively nascent industry with a near-term need for rapid deployments and prototype testing but also developers could see long-term benefits from the broad variety of materials available. AM also offers the unique ability to manufacture complex geometries that AM technologies offer.

Over the past 4 years, AM materials have played an increasing role in the Marine Energy Advanced Materials project—a multiyear, multilaboratory research project funded by the U.S. Department of Energy's Water Power Technologies Office (WPTO). The main goal of the project is to reduce barriers to the adoption of complex materials in the MRE industry. The primary focus of this project is to develop test methods and generate datasets to understand the long-term performance of advanced materials in marine environments and address specific material challenges as they arise. This report provides an extensive overview of the research that has been performed specific to AM polymers as part of the Advanced Materials project.

The intention of this document is to provide recommendations of best practices with regards to material selection, mechanical test method development, design practices, lessons learned along the way, current research trends, and ongoing challenges with regards to AM polymers in marine environments. In particular, this report focuses on several key aspects:

- Material and process selection
- Environmental conditioning and subsequent degradation quantification through mechanical characterization
- Composite reinforcements on AM polymer substrates
- Adhesion of instrumentation for mechanical characterization and loads measurements
- Protective coatings for preventing biofouling and water ingress
- Other MRE case studies where AM has proved particularly useful.

Ultimately, we hope that the test methods that have been developed, data generated, and lessons learned from this research will be valuable to both MRE researchers and developers alike, as well as to other industries. It can be used as a reference point as the respective MRE and AM industries continue to grow and mature.

Table of Contents

List of Figures

List of Tables

1 Introduction

The world's oceans and rivers offer an abundant source of energy in the form of currents and waves (Jacobson, Hagerman, and Scott 2011). Therefore, there is a large effort to develop technologies to convert this energy into clean, usable forms for utility-scale power generation or powering remote communities, aquacultures, desalination, and ocean exploration (Neary et al. 2014). The marine renewable energy (MRE) industry is still relatively nascent and facing a lot of challenges, with regards to reliability and economic feasibility. MRE devices are typically highly loaded structures that have to endure the harsh ocean environment (Figure 1). This issue is particularly challenging from a materials and manufacturing perspective. In ocean environments, polymers, especially fiber-reinforced polymers (FRPs), degrade and metals corrode; hence, material selection and understanding are critical to successful deployments. Additionally, appropriate manufacturing processes and the resulting material quality are closely tied to structural reliability and final costs.

The Marine Energy Advanced Materials project is an ongoing multiyear, multilaboratory effort to carry out industry-driven materials research to reduce barriers to the adoption of advanced materials in the MRE industry, such as FRPs, metals (and their interactions with other materials), antifouling paints, and additive manufacturing (AM) materials. This research includes:

- Industry surveys and workshops (WPTO 2022a)
- Understanding environmental degradation at the material level (Miller et al. 2020)
- Developing openly available mechanical degradation property datasets (Mandell et al. 2016)
- Assessments of biofouling and antifouling paints (Hernandez-Sanchez and Bonheyo 2017)
- Corrosion interactions between metals and FRPs (Abdulsalam and Presuel-Moreno 2021)
- Advanced instrumentation techniques (Murray et al. 2023)
- Subcomponent validation and test method development (Murdy, Hughes et al. 2023a)
- Understanding critical design details, such as FRP bolted and adhesive connections (Murdy, Hughes et al. 2023b)
- Understanding how coupon-scale mechanical degradation data can be implemented into the MRE design process at larger scales
- Advanced manufacturing processes, such as AM (Murdy, O'Dell et al. 2023).

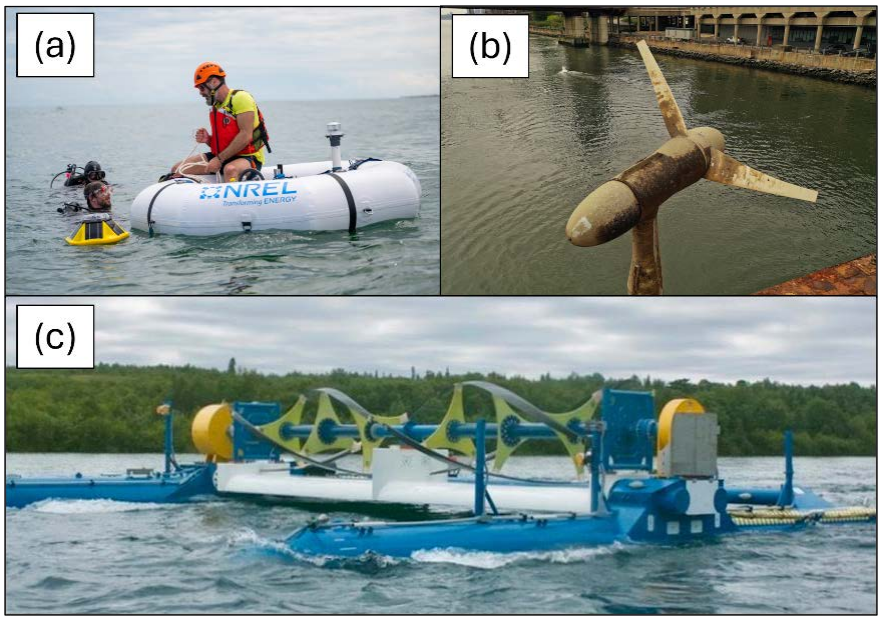

Figure 1. Examples of material challenges that MRE devices must endure: (a) the National Renewable Energy Laboratory's hydraulic and electric reverse osmosis wave energy converter, deployed in an area that can be subject to hurricanes, (b) a Verdant Power turbine with biofouling after deployment, and (c) the Ocean Renewable Power Company's RivGen Power System being installed on the Kvichak River in Igiugig, Alaska, where the river freezes in the winter

(a) Photo from John McCord, Coastal Studies Institute. (b) Photo from Paul Komosinski. (c) Photo from the Ocean Renewable Power Company and the Igiugig Village Council.

AM technologies have been rapidly maturing over the last decade. Originally, AM was primarily for the prototyping of components, with limited materials and access to high-quality systems. Now, a variety of AM technologies are much more accessible and offer the ability to manufacture final components at large scales, with a variety of advanced materials (e.g., thermoplastics, thermosets, FRPs, and metals), higher throughputs, and greater cost-effectiveness. For example, AM technologies have been used to manufacture wind turbine blade molds (Figure 2) (Post et al. 2017a), core materials for composite sandwich structures (Carron et al. 2023), soluble composite tooling (Türk et al. 2018), small-scale wind turbine blades (Bassett, Carriveau, and Ting 2015), and concrete structures, such as wind turbine towers (Jones and Li 2023).

Figure 2. A 13-meter wind turbine blade mold that was 3D-printed with chopped carbon fiber/acrylonitrile butadiene styrene, manufactured by Oak Ridge National Laboratory and TPI Composites

Photo by Ryan Beach, NREL

Therefore, there is great interest in understanding how AM processes and materials can be utilized in the MRE industry, not only for prototyping but also for manufacturing final components at scale. This interest is highlighted among the advanced materials and manufacturing research priorities for foundational R&D of WPTO's Multi-Year Program Plan (WPTO 2022b). AM has many current and potential uses in MRE technology development, such as for the quick iteration of models for laboratory-scale tow tank, flume, and wave tank testing, composite tooling, small component manufacturing, and full-scale structural components for deployment. There are many challenges associated with introducing new materials and manufacturing processes to a new industry, such as mechanical characterization, manufacturing defects, and compatibility with other materials and components. Therefore, AM processes and materials were introduced to the Advanced Materials project as a seedling project in 2020, with the goal of building a foundational understanding of these challenges and how AM can be reliably implemented into MRE components and structures. This research has continued through 2024.

This report provides a deep dive into the polymer AM research that has been performed over the past 4 years and its progression as part of the Advanced Materials project. That work includes:

- AM process and material selection
- Characterization of mechanical properties and environmental degradation
- Unique composite manufacturing approaches and adhesion of composite reinforcements
- Instrumentation
- Protective coatings (antifouling paints and water ingress prevention)
- Other applications and case studies beyond the AM project
- Future research directions

We anticipate that the data generated and lessons learned from this research will be incredibly valuable to both the MRE community (researchers and developers alike) and other industries and are being disseminated as such.

2 Process and Material Selection

There are many AM processes and materials available on the market today, which makes selecting the optimum process and material for a given component particularly challenging. This selection is especially important for MRE systems, where device architectures vary considerably between developers, who all have their own unique requirements. Therefore, robust process and material selection processes are a necessity. There are many considerations to be made when selecting a manufacturing process, such as capital costs, scalability, and postprocessing requirements. Material selection may be more focused on mechanical properties, such as stiffness, strength (static and fatigue), and resistance to environmental degradation. The importance of these requirements and properties is application-dependent.

To account for the many processes, materials, and properties, a decision matrix (or Pugh matrix) approach is common for material selection. Properties and requirements are weighted based on their importance to the application, and then materials and processes are scored based on how well they fit the criteria. A total score is then calculated as the summation of the individual requirements' weighted scores. Because the available AM materials and their mechanical properties may vary significantly with the AM process selected, it may be necessary to first consider processes and materials separately and then combine scores.

Gonzalez-Montijo et al. (2023) took this combined approach when determining the ideal AM process and materials for a 3D-printed tidal turbine blade spar (Figure 3). AM processes and materials were assessed separately, and then combined scores were calculated to determine the optimum AM process and material (Table 1 and Table 2). Computer numerical control (CNC) machining and aluminum 6061 were also scored as baselines for comparison. In this case, direct energy deposition (DED) and 316L stainless steel were chosen for the final AM manufacturing process and material, respectively. Although polymeric materials were not selected in this case, it still highlights the approach to process and material selection. Readers will notice that fused deposition modeling (FDM) scored highest in terms of AM processes (Table 1), but it was not chosen once the material properties had been considered and the total scores were calculated (Table 2), thus highlighting the importance of considering processes and materials together.

Figure 3. Structural validation of a 3D-printed tidal turbine blade spar manufactured using DED and 316L stainless steel

Photo by Paul Murdy, NREL

Table 1. An Example AM Process Decision Matrix for the 3D-Printed Tidal Turbine Blade Spar

Data from Gonzalez-Montijo et al. (2023)

Requirement	Weight	CNC Machining	FDM	DED
Capital cost	3	-1	2	1
Deposition rate	2	0	2	1
Surface finish	3	1	-1	-1
Resolution	1	1	0	-1
Postprocessing	3	2	0	0
Material options	2	1	1	2
Porosity	1	2	-2	2
Ease of feature integration	2	-1	2	1
Scalability (size)	4	0	2	2
Scalability (performance)	3	1	1	2
Accessibility	2	2	2	1
Total Score		**16**	**26**	**25**

Table 2. An Example AM Material Decision Matrix for a 3D-Printed Tidal Turbine Blade Spar With Combined Process/Material Scores

Data from Gonzalez-Montijo et al. (2023)

Requirement	Weight	CNC Machining–Al 6061-T6	FDM–Chopped-Carbon ABS[a]	FDM–Ultem	DED–316L Stainless Steel	DED–Ti-6Al-4V
Static strength	3	1	-1	-1	1	2
Fatigue strength	3	0	1	1	1	1
Elastic modulus	4	0	-1	-1	2	1
Density	1	0	2	2	-2	-1
Environmental resistance	4	1	2	2	1	2
Ultraviolet resistance	2	2	-1	2	2	2
Toughness	3	2	0	0	2	1
Cost	2	-1	2	1	1	-2
Total Score		**15**	**9**	**12**	**25**	**23**
Combined Process/Material Score		**31**	**35**	**38**	**50**	**48**

[a] Acrylonitrile butadiene styrene.

It should be noted that the decision matrix approach is not perfect and is highly dependent on user inputs and their biases. Sensitivity analyses should also be performed to fully understand the effects of the most important variables. The described approach is just one example of AM process and material selection for an MRE component. Ultimately, no process or material is perfect for any one application. Each process and material has advantages and disadvantages—it is up to the user to determine what is optimum for the application.

3 Mechanical Properties and Environmental Degradation

It is well known that the thermomechanical and mechanical properties of polymeric materials degrade over extended periods of time in water (Shen and Springer 1976). If AM polymers are to be used for MRE components, then understanding how their mechanical properties degrade over time and how to properly quantify said degradation in a controlled laboratory setting is a key aspect of the successful selection of AM polymers and their implementation into MRE designs.

To properly assess AM polymers for marine environments, researchers must consider test methods for environmental conditioning and mechanical test methods to quantify the degradation resulting from environmental conditioning. This practice is common for FRPs; however, our research found that AM polymers come with their own unique considerations when applying these test methods.

3.1 Environmental Conditioning Approaches

In-water environmental conditioning is often used as a precursor to mechanical characterization to quantify environmental degradation, but it can also be used to measure water absorption properties during the conditioning process. Polymers absorb water on a molecular level, which is often associated with Fickian diffusion (Shen and Springer 1976). Water molecules pass between the polymer chain networks and work their way through the bulk polymer until it becomes fully saturated. This is a gradient- and material-dependent process that can be measured during environmental conditioning to evaluate diffusion coefficients and maximum water uptake (m_∞) values.

For bulk polymers and FRPs, ASTM D5229 Standard Test Method for Moisture Absorption Properties and Equilibrium Conditioning of Polymer Matrix Composite Materials Procedures A and B are commonly used for ambient and nonambient determination of Fickian moisture diffusion properties. Specimens are typically thin and flat to allow for a one-dimensional diffusion assumption to be made. Usually, mechanical test specimens are already cut to their final dimensions for subsequent mechanical characterization. Specimens can be conditioned at ambient temperatures; however, the experiment would not be accelerated, i.e., 6 months of conditioning would only equate to 6 months of in-service conditions. This situation may be acceptable in some cases but may not be acceptable for materials that need to be in service for extended periods of time (>1 year). In that case, water temperatures are elevated to accelerate the environmental degradation process; however, equating these accelerated timescales to real time in service can be unreliable (Murdy, Hughes et al. 2023b). Often, data from elevated temperature testing are used as a worst-case scenario.

Determining the appropriate temperature for accelerated environmental conditioning is an important consideration. ASTM D5229 states that conditioning temperatures should be at least 25°C below the wet glass transition temperature (T_g) of the material being tested. For AM polymers, this may be a challenge for two reasons:

1. The wet T_g of the material is likely unknown. T_g typically decreases due to the water absorption process.

2. Most AM polymers are thermoplastics and may have a relatively low T_g when compared with thermoset FRPs, which limits the maximum allowable conditioning temperature and makes it difficult to sufficiently accelerate the conditioning process.

During the environmental conditioning, specimens should be weighed periodically to track changes in mass (or water absorption) for the prescribed conditioning period or until the mass measurements plateau. Diffusion coefficients and m_∞ can be determined from the datasets.

3.1.1 Ambient Environmental Conditioning

In collaboration with Pacific Northwest National Laboratory, a benchmark environmental degradation study was conducted on some AM polymers manufactured using FDM. Materials were selected based on a combination of internal manufacturing capabilities and their mechanical and environmental resistance properties. Table 3 shows a summary of the chosen materials. Specimens were cut or printed into standard mechanical test geometries prior to conditioning (Figure 4). Section 3.2.1 provides more details on the chosen geometries.

Table 3. Summary of Materials Chosen for the Ambient Environmental Conditioning Study with Pacific Northwest National Laboratory

Data from Murdy, O'Dell et al. (2023)

Material	AM Process	Defining Characteristics
Acrylonitrile styrene acrylate	FDM	Low cost, environmental resistance
Ultem 9085[a]	FDM	High environmental resistance
Onyx[b]	FDM	Moderate stiffness and strength
Carbon-fiber-reinforced Onyx[b]	Continuous-fiber FDM	High stiffness and strength
Glass-fiber-reinforced Onyx[b]	Continuous-fiber FDM	Low cost, high stiffness and strength

[a] Polyetherimide blend from Stratasys.

[b] Chopped-carbon-fiber-reinforced nylon from Markforged.

Figure 4. Photo of specimens used in the ambient environmental conditioning study with Pacific Northwest National Laboratory

Source: Murdy, O'Dell et al. (2023)

Specimens were conditioned at ambient temperatures in Pacific Northwest National Laboratory's ocean water conditioning tanks at the Marine and Coastal Research Laboratory in Sequim, Washington (Figure 5). Untreated seawater was regularly circulated, allowing marine organisms to grow and interact with the test specimens for a variety of biofouling, corrosion, and degradation studies. The average temperature in the tanks was ~12°C. Specimens were conditioned for a total of 155 days before being returned to the National Renewable Energy Laboratory (NREL) for mechanical characterization.

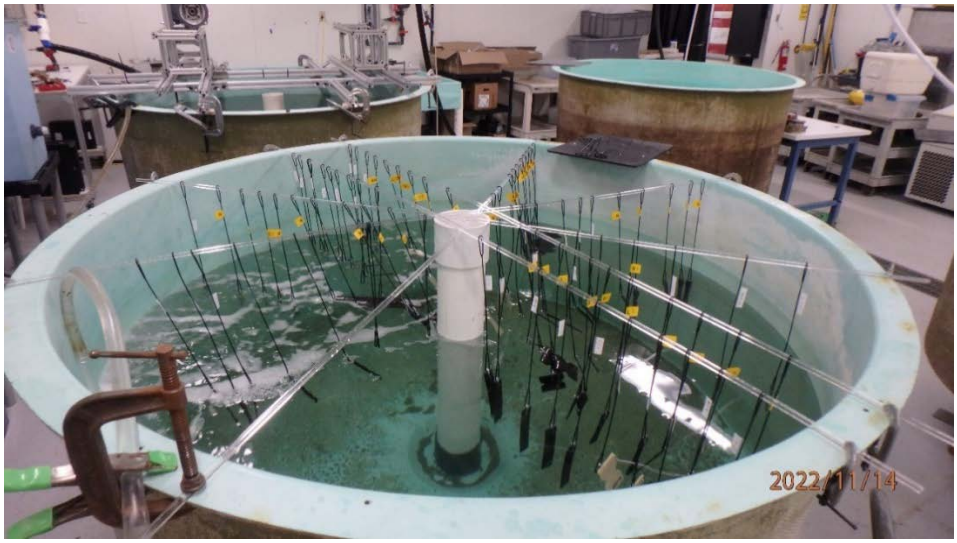

Figure 5. Specimens suspended in one of Pacific Northwest National Laboratory's seawater conditioning tanks

Source: Murdy, O'Dell et al. (2023)

The specimen masses were not measured periodically; therefore, no Fickian coefficients were calculated in this study. The masses were measured only before and after environmental conditioning. The specimens were wiped clean of any biofouling prior to the mass measurements. Figure 6 shows the mass change results for the materials and various ASTM specimen geometries. Readers can find the full discussion of these results in Murdy, O'Dell et al. (2023); however, the key takeaways are as follows:

1. The standard deviations were large. Measurements may have been affected by biofouling and water trapped within the pores of the 3D prints. Materials manufactured using FDM have a very porous structure, which is dependent on the printer nozzle size, deposition rate, and tool paths.
2. Conditioning specimens in distilled water may have yielded more consistent results. It is generally understood that salts have negligible effects on polymer degradation but can be a source of error in mass measurements. Therefore, distilled water is often preferred for environmental conditioning studies on FRPs (Miller et al. 2020).
3. Acrylonitrile styrene acrylate (ASA) and Ultem 9085 were similar in their mass change trends.
4. The mass changes for Onyx varied considerably with the specimen geometry.

5. Continuous-carbon and glass-fiber-reinforced Onyx gained significantly more mass than did the other materials. We suspect this is due to water being wicked along the continuous fibers by capillary action.
6. No notable visual changes were observed for any of the materials tested.

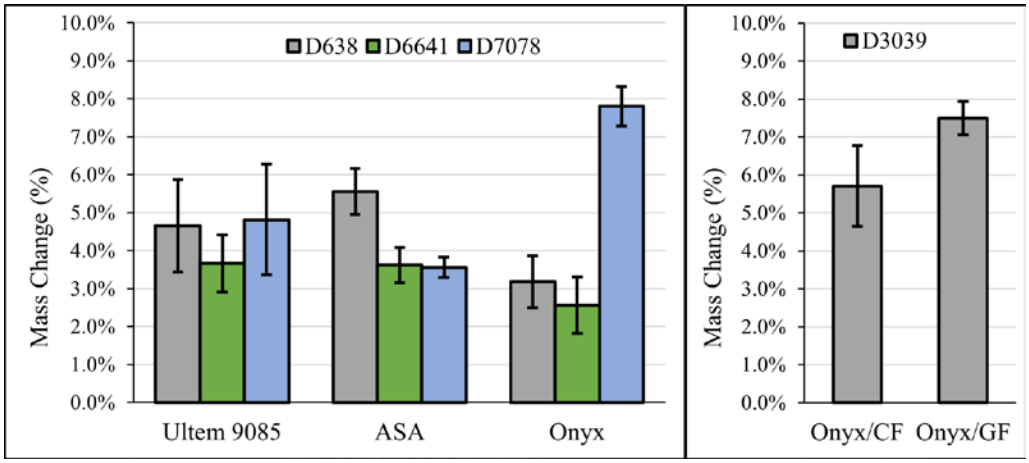

Figure 6. A comparison of measured mass changes for the materials conditioned at Pacific Northwest National Laboratory

Source: Murdy, O'Dell et al. (2023). CF = carbon fiber; GF = glass fiber.

3.1.2 Accelerated Environmental Conditioning

In parallel with the environmental conditioning study performed in section 3.1.1, Montana State University performed an accelerated environmental conditioning study for comparison. That study used the same 3D-printed polymers and specimen geometries as in the other study. The specimen geometries were thoroughly documented to evaluate their dimensional tolerances and any specific nonuniformities, which may impact the results of the study discussed in this section and those presented in section 3.2.2. In particular, both curvature and nonflat, parallel surfaces were noted for the continuous-carbon and glass-fiber-reinforced Onyx D3039 specimens (Figure 7). These variations appeared to be induced by the Markforged printing process, which involves nonuniform residual thermal stresses when printing layer by layer, exacerbated by the significantly different mechanical properties of the continuous-fiber reinforcements.

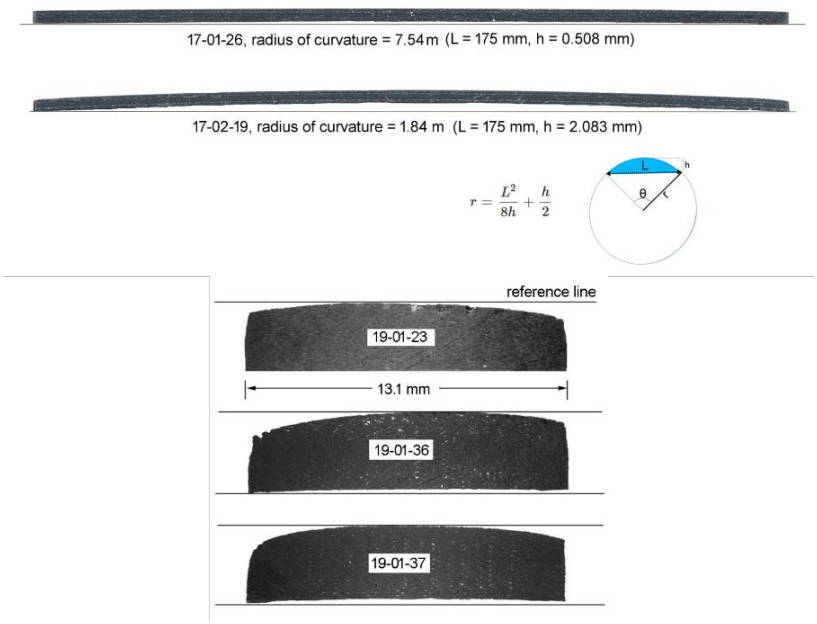

Figure 7. Curvature (top) and nonuniform cross-sectional area (bottom) of the unconditioned, continuous-fiber-reinforced Onyx specimens

Image by Daniel Samborsky, MSU. m = meter; *L* = length; *h* = height; mm = millimeter; *r* = radius.

Figure 8 shows photos of the front faces of the test specimens, detailing the voids between the filament passes. The ASA, Ultem 9085, and Onyx photos at the top of Figure 8 depict the full specimen widths (~12.7 millimeters [mm]), whereas the continuous-fiber constructions are magnified to show the voids and filament passes. Table 4 presents the measured densities and fiber volume contents. The fiber volume was measured via measuring the fiber surface area using micrographs and by the matrix digestion (or burn-off) method in an oven at 650°C. The continuous and random carbon fiber present in the constructions survived the high temperatures in the matrix digestion method without the aid of a protective atmosphere (Figure 9).

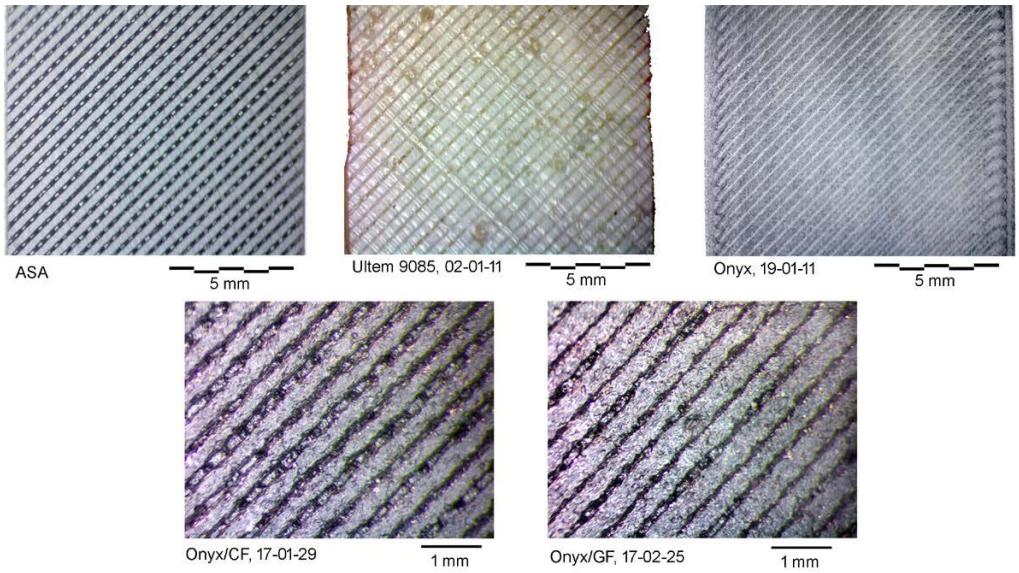

Figure 8. Front faces of the test materials, exhibiting a repetitive pattern of ridges and valleys due to the layer-by-layer deposition process. That process results in a surface that can be relatively rough, with many voids.

Photos by Daniel Samborsky, MSU. CF = carbon fiber; GF = glass fiber.

Table 4. Measured Densities and Fiber Volume Fractions of Unconditioned Materials.

Material	Measured Density (g/cm^3)[a]	Measured V_f[b] (%)	Measured area % of different phases (micrograph)
Ultem 9085	1.13	-	-
ASA	0.98	-	-
Onyx	1.13	-	-
Onyx/Carbon Fiber	1.12	9.4	11.1[c]
Onyx/Glass Fiber	1.14	6.7	13.3[c]

[a] Grams per centimeter cubed.

[b] Volume fraction.

[c] Micrographs showed continuous fibers with additional chopped carbon fibers at random orientations.

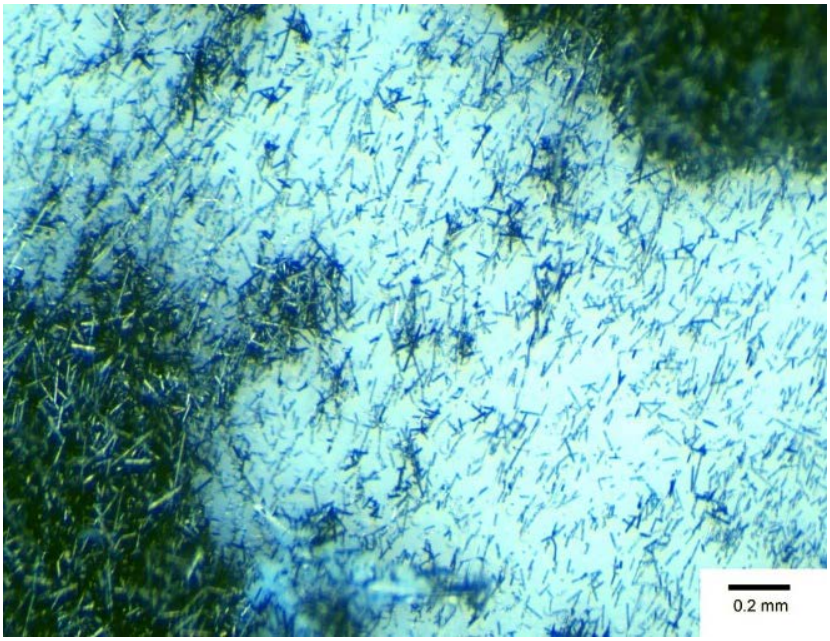

Figure 9. Photo of residual short carbon fibers present after matrix digestion in the Onyx materials

Photo by Daniel Samborsky, MSU

We placed one half of the specimens from each series in a distilled water bath at 50°C for a period of 365 days to ensure full saturation. The conditioning temperature was determined based on the T_g of the materials (Table 5). Periodic removal of the specimens for interim moisture uptake weighing yielded erratic readings with the drying methods employed. Those methods involved removing the specimens from the water baths, blotting them dry with paper towels, exposing them to room air with light air flow for 15 minutes (min) to evaporate any water left in the surface voids, and then weighing them on a Cole-Parmer PA-220 (220 grams by 0.0001 gram) laboratory balance. Water present in surface-accessible pores was difficult to remove to get an accurate and repeatable moisture measurement. We tried various specimen-drying methods, such as vacuum drying at room temperature and/or drying under standard dry room air circulating over the specimens, to get a weight gain versus soaking time dataset. Results were highly variable, so more research is needed to determine optimum and reliable test procedures that account for all the liquid water present. With the moisture mass variability, we decided to just take a final value under full moisture saturation after an extended soaking time. Figure 10 details the mass change over a 24-hour period from full saturation for the different test series specimens. The speed of weight loss in this short period of time suggests the presence of huge cavities of water, even after exposure to dry-air conditions. The long periods of drying time to get true moisture uptake values could also have resulted in the removal of diffused moisture from the material while also leaving liquid water in deep interior pores. We took micrographs to evaluate the pores within the materials tested (Figure 11). The current testing protocol violates a main assumption of the ASTM D5229 standard test method, specifically section 6.3.7 of that method, where any materials containing an abnormal number of voids or amount of porosity will exhibit non-Fickian material behavior. To get more accurate and truthful moisture uptakes for a diffusion curve, higher-density material forms with lower void contents are necessary. More research for weighing procedures needs to be performed in this area.

Table 5. The Wet Glass Transition Temperatures (T_g) of the Materials Subjected to Accelerated Environmental Conditioning

Material	T_g (°C)
Ultem 9085	186
ASA	112
Onyx	105
Onyx/Carbon Fiber	105
Onyx/Glass Fiber	105

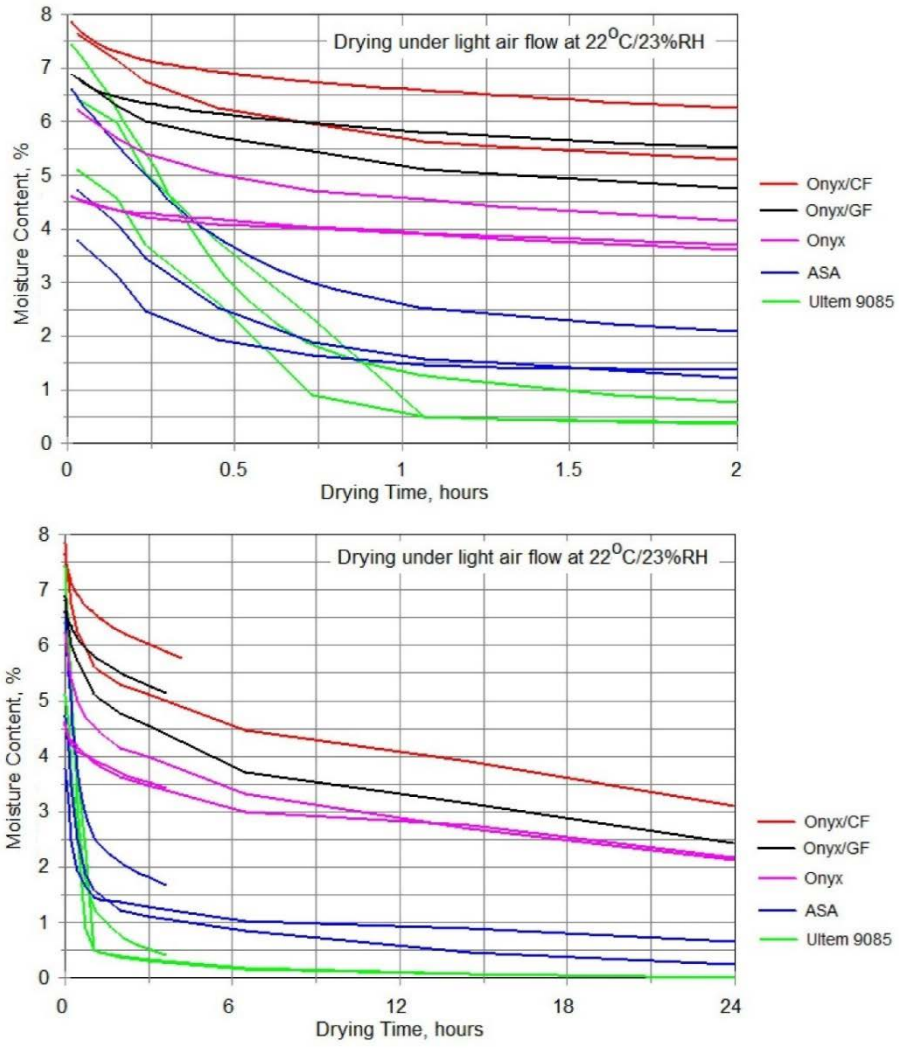

Figure 10. Moisture content versus drying time for vertically suspended specimens in light airflow, beginning 1 min after being blotted dry from a fully saturated condition

Image by Daniel Samborsky, MSU. RH = relative humidity; CF = carbon fiber; GF = glass fiber.

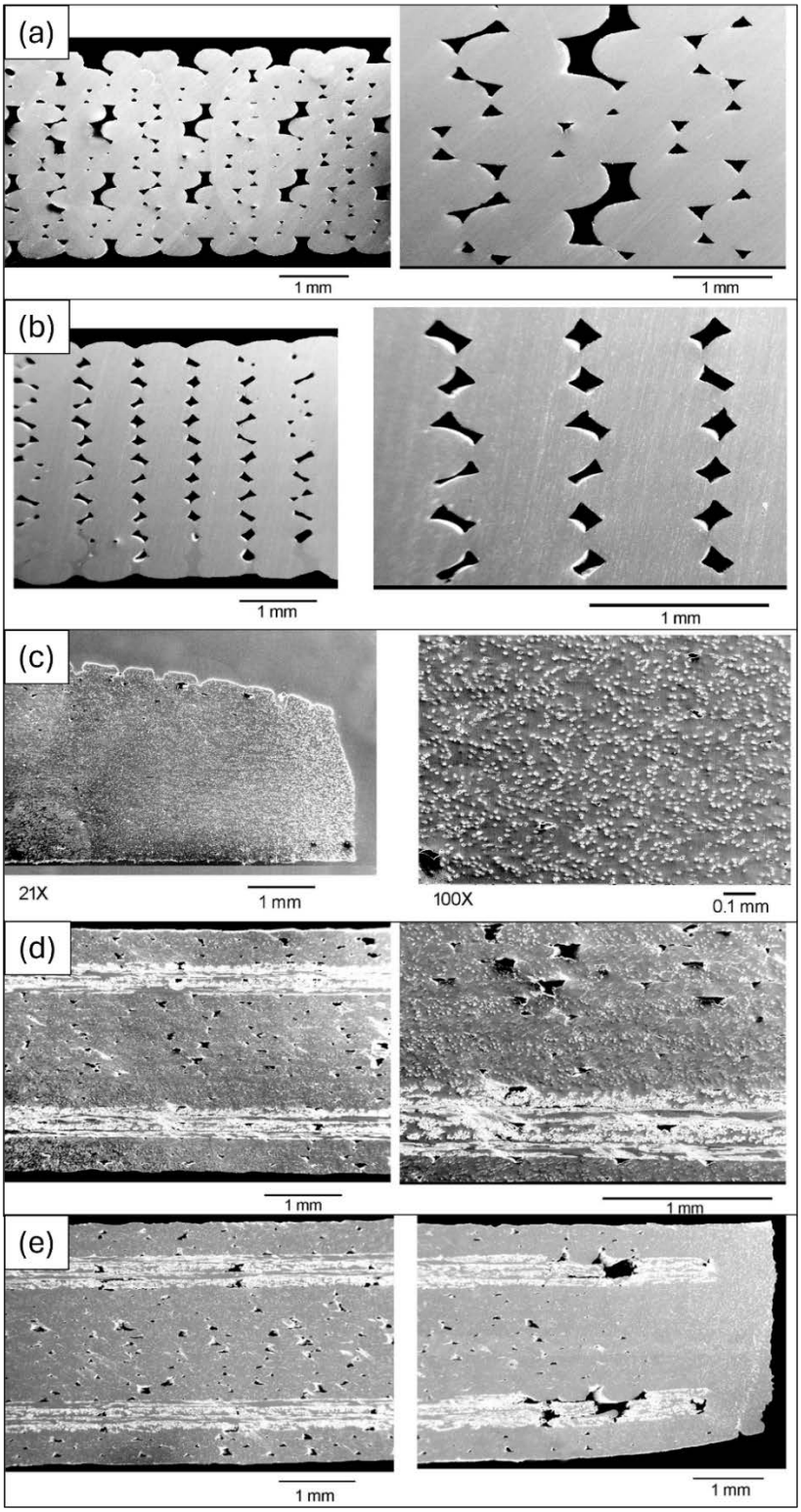

Figure 11. Micrograph images showing the porosity of the materials tested: (a) Ultem 9085, (b) ASA, (c) Onyx, where the white dots are the chopped-carbon-fiber reinforcement, (d) Onyx/carbon fiber, where the white streaks are the continuous fibers, and (e) Onyx/glass fiber, with the white streaks showing the continuous fibers

Image by Daniel Samborsky, MSU

Figure 12 shows the percentage mass changes for the D638, D7078, and D3039 specimens that were environmentally conditioned at elevated temperatures. The specimens were air dried for 1 hour prior to final weighing. The trends between the results were similar to those presented in Figure 6; however, readers should note that the absolute values vary significantly due to the differences in the final drying procedures that were used.

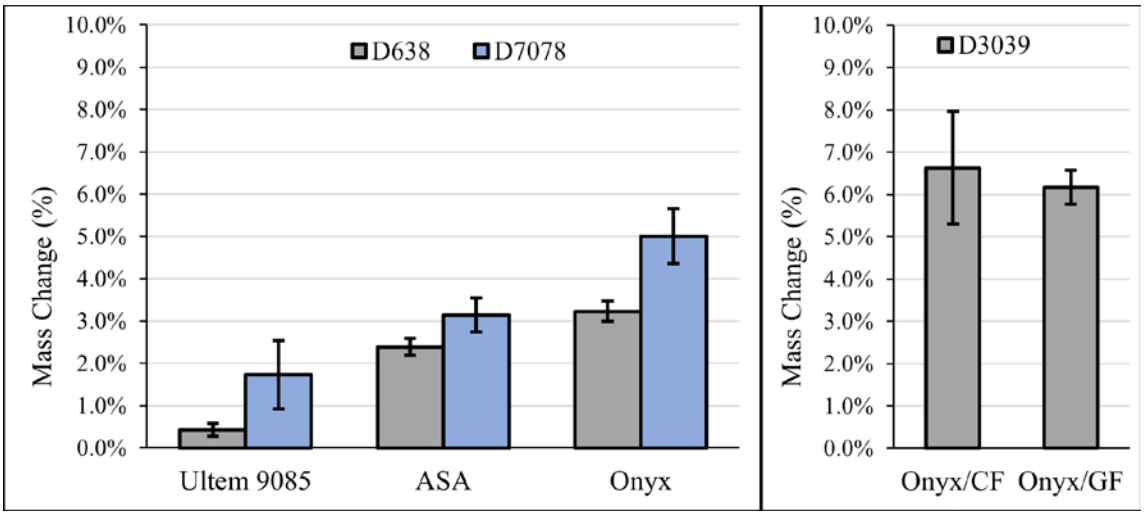

Figure 12. A comparison of percentage mass changes for specimens that were fully saturated after environmental conditioning at elevated temperatures (error bars represent standard deviations)

Image by Daniel Samborsky, MSU. CF = carbon fiber; GF = glass fiber.

Finally, Figure 13 shows a comparison of measured dry and saturated thickness changes for the materials and specimen geometries tested. Most notable are the Onyx and continuous-fiber-reinforced Onyx specimens that were tested. In fact, the continuous carbon and glass fiber specimens swelled up like a balloon due to liquid water existing between the fibers and the adjacent plies, creating a delamination plane.

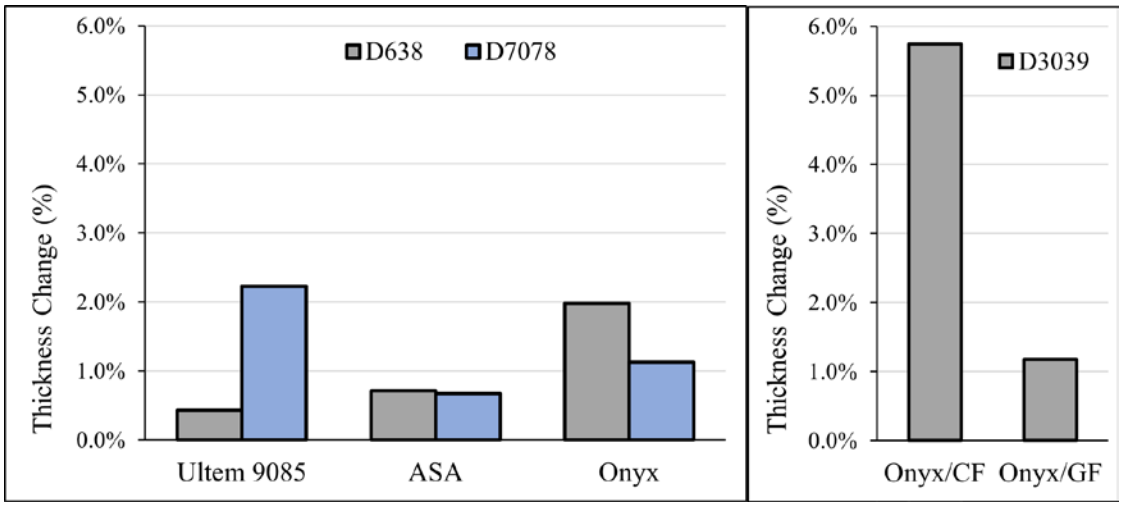

Figure 13. Comparisons of percent thickness changes for the dry and fully saturated test specimens

Image by Daniel Samborsky, MSU. CF = carbon fiber; GF = glass fiber.

3.2 Mechanical Characterization

To qualify materials for use in marine environments, it is prudent to compare their mechanical properties before and after environmental conditioning. The extent of mechanical characterization required will depend on the structural significance of the component and the calculated risks associated with failure. In some cases, this approach may be as simple as comparing dry and wet tensile strengths to verify that the material is suitable for low-stress states or limited deployment times. For more critical components and longer deployment times, more in-depth characterization of environmental effects may be necessary to properly account for them in mechanical designs.

AM (or 3D-printed) materials are typically anisotropic because they are manufactured layer by layer. Parts manufactured using filament-based techniques, such as FDM, can be more complex because mechanical properties vary based on the filament direction. Currently, there are no dedicated mechanical testing standards for as-manufactured 3D-printed materials. Therefore, selecting the most appropriate testing standards can be challenging. Current research appears to apply a variety of plastic and FRP test standards to characterize and compare as-manufactured mechanical properties even when fiber reinforcements are not present (Kim and Kang 2020). The studies in the next sections outline the findings and challenges of several ASTM test methods applied to the materials conditioned in sections 3.1.1 and 3.1.2. The performances of the materials in marine environments are compared.

3.2.1 Post-Ambient Environmental Conditioning

The dry and conditioned materials outlined in section 3.1.1 were compared using the following ASTM standard test methods:

- ASTM D638 Standard Test Method for Tensile Properties of Plastics (ASA, Ultem 9085, and Onyx)
- ASTM D6641 Standard Test Method for Compressive Properties of Polymer Matrix Composite Materials Using a Combined Loading Compression Test Fixture (ASA, Ultem 9085, and Onyx)
- ASTM D7078 Standard Test Method for Shear Properties of Composite Materials by V-Notched Rail Shear Method (ASA, Ultem 9085, and Onyx)
- ASTM D3039 Standard Test Method for Tensile Properties of Polymer Matrix Composite Materials (continuous glass- and carbon-fiber-reinforced Onyx).

For the ASA and Ultem 9085 materials, specimens were cut from larger panels to measure bulk, homogeneous properties with minimal influence from the filament directions. The same was attempted for the Onyx and fiber-reinforced Onyx specimens; however, processing the bulk material presented significant challenges. It appeared that the interlaminar strength of the material was minimal, resulting in significant delaminations from both CNC machining and waterjet cutting. Therefore, the specimens were printed individually; hence, the measured dry and conditioned mechanical properties were used for comparative purposes only.

The specimens were instrumented with foil strain gages and extensometers to measure changes in strain during the testing (Figure 14). Figure 15 and Figure 16 show comparisons of the dry and conditioned moduli and strengths measured during the study.

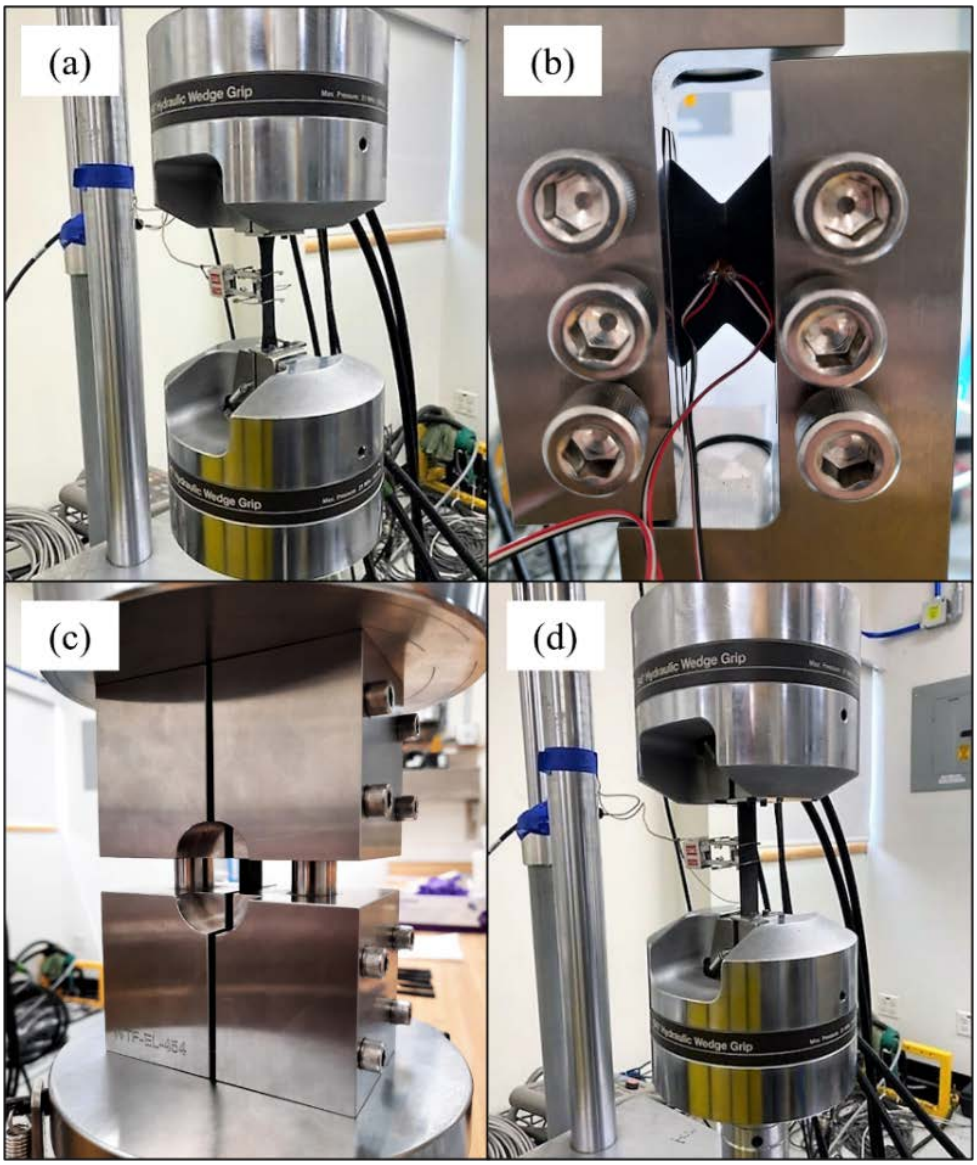

Figure 14. Examples of the test methods applied: (a) ASTM D638 tension, (b) ASTM D7078 shear, (c) ASTM D6641 compression, and (d) ASTM D3039 tension

Source: Murdy, O'Dell et al. (2023)

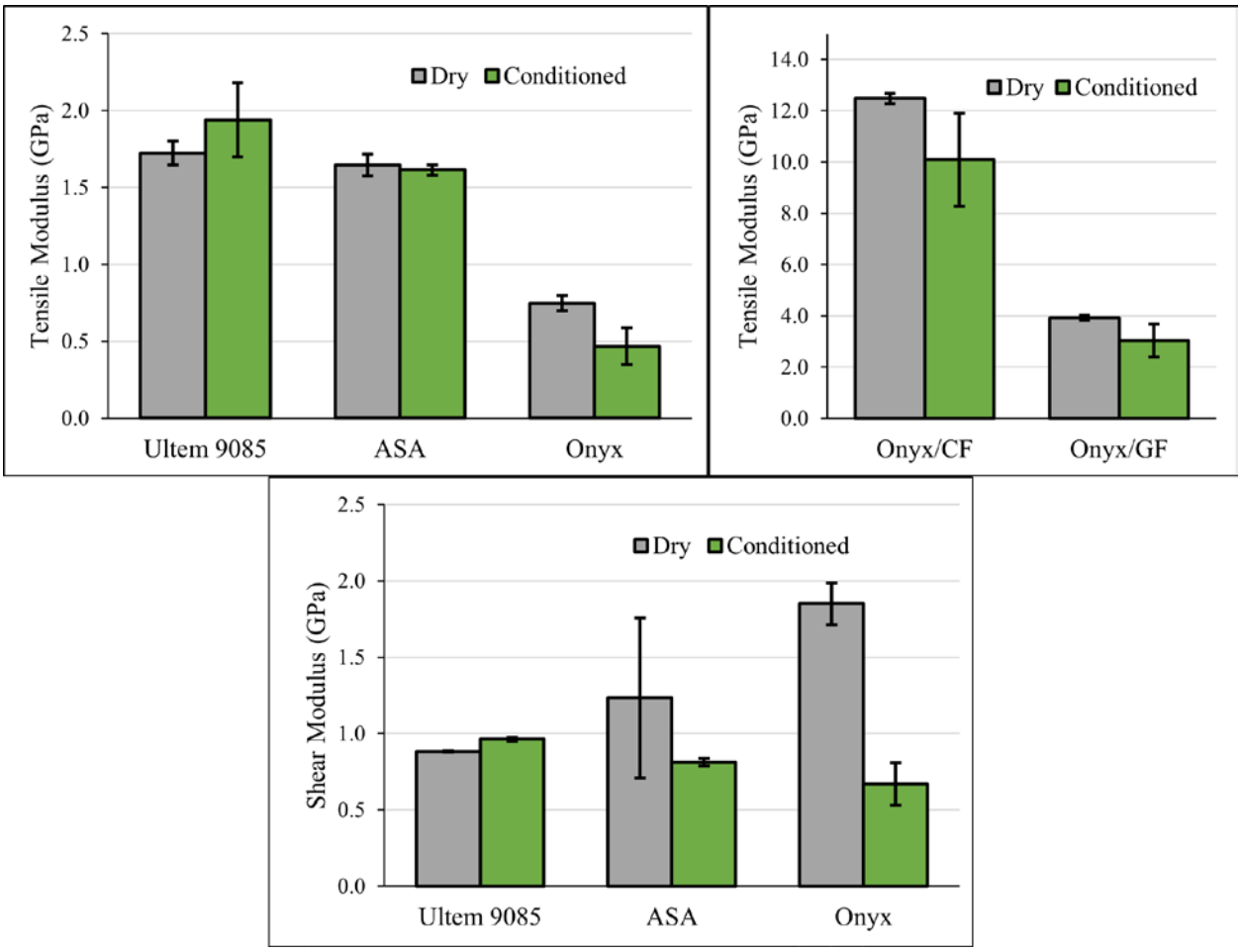

Figure 15. Comparisons of dry and conditioned moduli for the materials tested

Source: Murdy, O'Dell et al. (2023). GPa = gigapascal; CF = carbon fiber; GF = glass fiber.

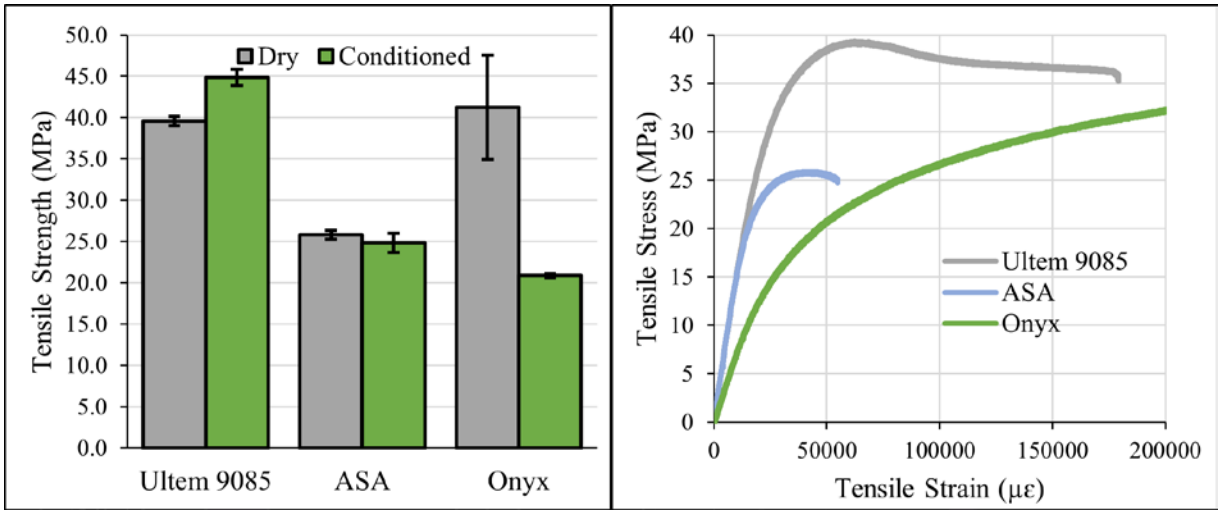

Figure 16. Comparisons of dry and conditioned tensile strengths using ASTM D638 (left), and example stress-strain plots from the dry specimen testing (right)

Source: Murdy, O'Dell et al. (2023). MPa = megapascal.

Further analyses, comparisons, and discussions of the datasets can be found in Murdy, O'Dell et al. (2023). However, the key takeaways can be summarized as follows:

- The tensile and shear moduli of the ASA and Ultem 9085 specimens were relatively unchanged due to the environmental conditioning.
- The Onyx and fiber-reinforced Onyx exhibited significant reductions in tensile and shear moduli (up to 65%).
- ASA and Ultem did not suffer any significant reductions in strength due to the ambient environmental conditioning.
- Onyx lost ~50% of its tensile strength, and the conditioned fiber-reinforced Onyx could not be compared; this was due to crushing in the load frame grips—attributed to significant losses in through-thickness strength.
- Compressive properties could not be compared because of excessive buckling owing to insufficient specimen thickness.
- **Adhesion of foil strain gages to the specimens was challenging. In some instances, gages peeled off before testing had started. Therefore, the efficacy of strain gage adhesives on 3D-printed polymers must be investigated further.**

Ultimately, the results showed that some 3D-printed polymers may perform significantly better than others in marine environments. Also, if the deployment period is short, it should not be assumed that the degradation will be minimal, as evidenced by the nylon-based Onyx results.

3.2.2 Post-Accelerated Environmental Conditioning

Continuing from section 3.1.2, dry and fully saturated specimens were subjected to similar mechanical testing following these ASTM standards:

- ASTM D638 Standard Test Method for Tensile Properties of Plastics
- ASTM D7078 Standard Test Method for Shear Properties of Composite Materials by V-Notched Rail Shear Method
- ASTM D3039 Standard Test Method for Tensile Properties of Polymer Matrix Composite Materials

Compression testing was neglected in this study due to the buckling issues noted in section 3.2.1.

The tensile testing was performed on an Instron 8562 servoelectric testing machine with a clip-on extensometer using a 25.4-mm gage length. Testing was performed at 22°C and 27% relative humidity. The elastic modulus was taken as the best-fit line between 0.1% and 0.3% strain on the stress-strain curve. Tensile and shear specimens were loaded with a displacement ramp rate of 1.5 mm/min. No strain data (and therefore modulus and strain-to-failure data) were recorded for the shear specimens due to the issues with the bonded strain gages noted in section 3.2.1. It was also noted that strain gage application could be problematic due to the rough surfaces of the 3D-printed materials. The strain gage grid needs to be fully supported against the specimen surface and average only those regions of the grid that are in contact with the surface. For better-quality strain measurements, voids will have to be filled with a compatible adhesive prior to strain gage bonding.

Figure 17 and Figure 18 show the dry and fully saturated comparisons from the tensile and shear testing, respectively. Figure 19 shows the tensile stress-strain data that the tensile properties were extracted from. Overall, the trends and absolute values of the datasets were comparable to the ambient conditioning study in the previous section, and similar conclusions can be made regarding the performance of the materials. Similar failure mechanisms were recognized for the specimens tested. Photos and micrographs of the specimen failures can be found in the Appendix. Additionally, similar issues were found regarding grip failures of the continuous-fiber-reinforced specimens and unrepresentative buckling failures of the Onyx V-notched shear specimens. For future mechanical characterization studies on 3D-printed materials, we have several recommendations to address these issues:

1. Tensile testing: Gripped material in the testing machine's metal wedge grips should ideally be 38–50 mm in length to reduce gripping stresses. Current ASTM D638 test geometries (dogbone) may work, but longer specimen lengths with more generous radii may be needed for good failure modes. The rectangular continuous-fiber specimens all failed at the grip interface to the gage section. Longer overall specimen lengths could employ longer tab material to reduce gripping stresses.
2. Compression testing: 3D-printed polymers have low moduli and low through-thickness properties, which promote early buckling. Compression tests were not performed in this study due to this problem. Cylinder or cube geometries could provide better and more consistent results, but this consideration needs to be researched to determine the best and most truthful procedure. The ASTM D695 standard would probably work better as a test geometry, where the test specimen height is twice its principal width or diameter, usually a prism of 12.7 × 12.7 × 25.4 mm, or a cylinder with a diameter of 12.7 mm and a height of 25.4 mm.
3. Shear testing: Out-of-plane deformations were present on the three materials tested, which changed the shear test to a tearing test. The Onyx specimens easily went into a tearing mode of failure. Thicker constructions should provide more resistance and promote a more consistent shear response.
4. Tighter tolerances and flatness on the constructed geometries would also provide more consistent testing results. In particular, the Onyx and continuous-fiber-reinforced Onyx specimens were visibly warped and had through-thickness curvatures (Figure 7) due to residual thermal stresses caused by the layer-by-layer FDM printing process. Because of this warping and curvature, gripping or load introduction into the gage sections was negatively affected and cross-sectional area calculations may not have been accurate. Additionally, the specimens' curvatures, when straightened out in a uniaxial test, will cause nonuniform strains on the opposing faces, which will influence the final test results and ultimate failures.

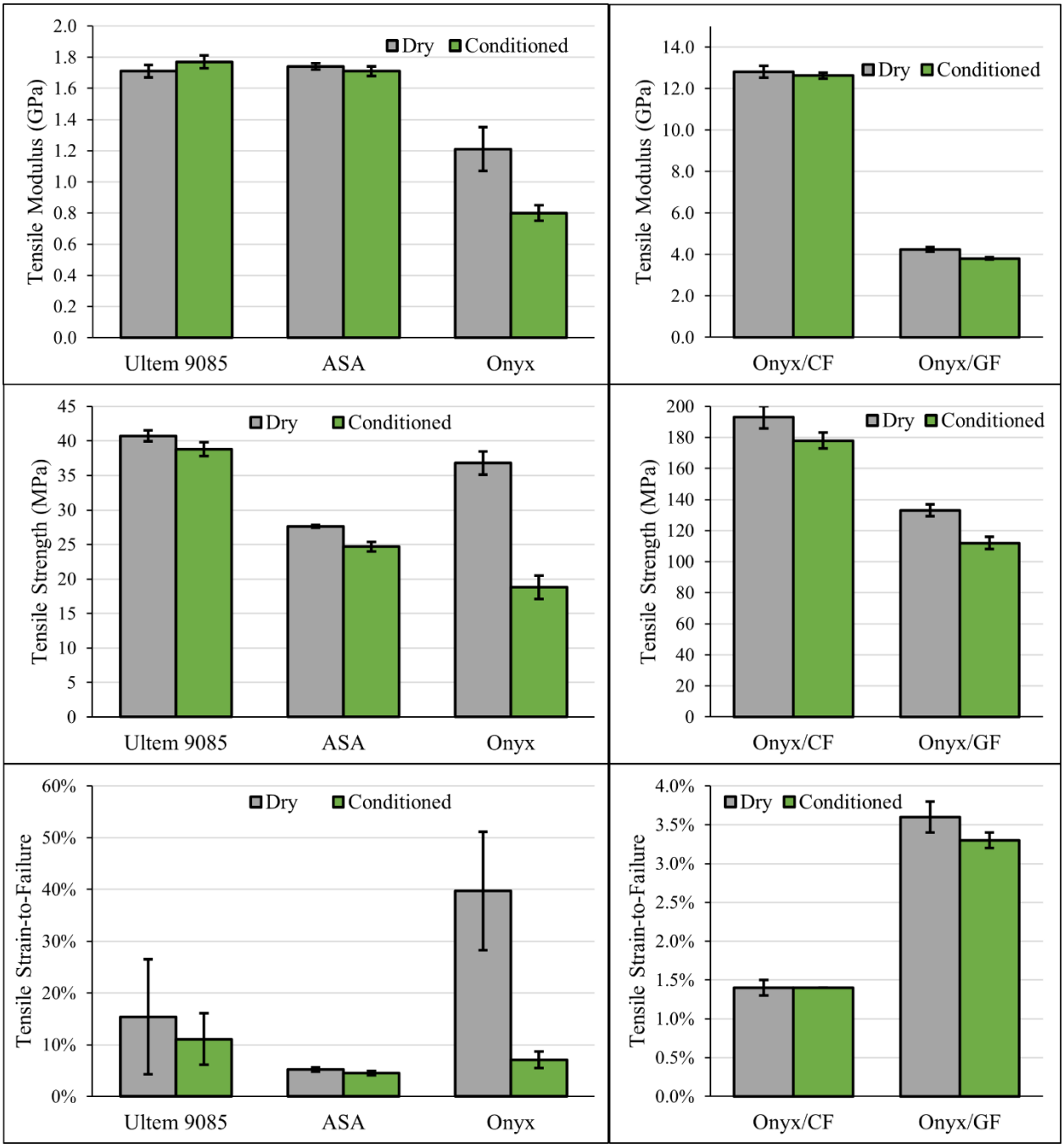

Figure 17. Dry and fully saturated (conditioned) comparisons of the tensile testing results: (top) tensile modulus, (middle) tensile strength, and (bottom) tensile strain-to-failure (error bars represent standard deviations)

Images from Daniel Samborsky, MSU. GPa = gigapascal; MPa = megapascal; CF = carbon fiber; GF = glass fiber.

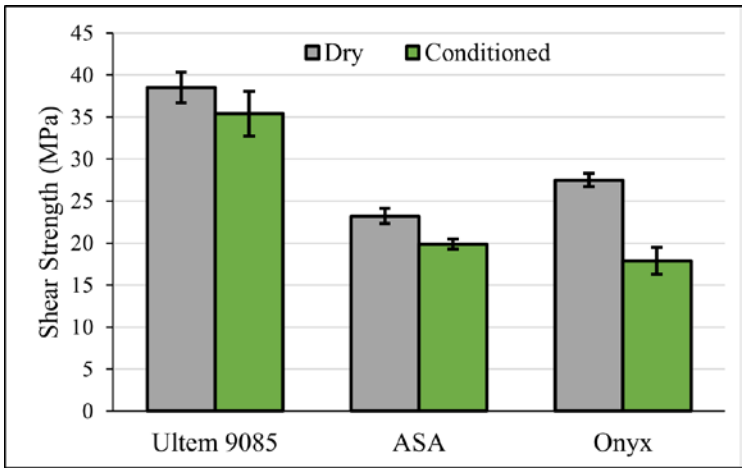

Figure 18. Dry and fully saturated (conditioned) comparisons of the recorded ultimate shear strengths (error bars represent standard deviations)

Image from Daniel Samborsky, MSU. MPa = megapascal.

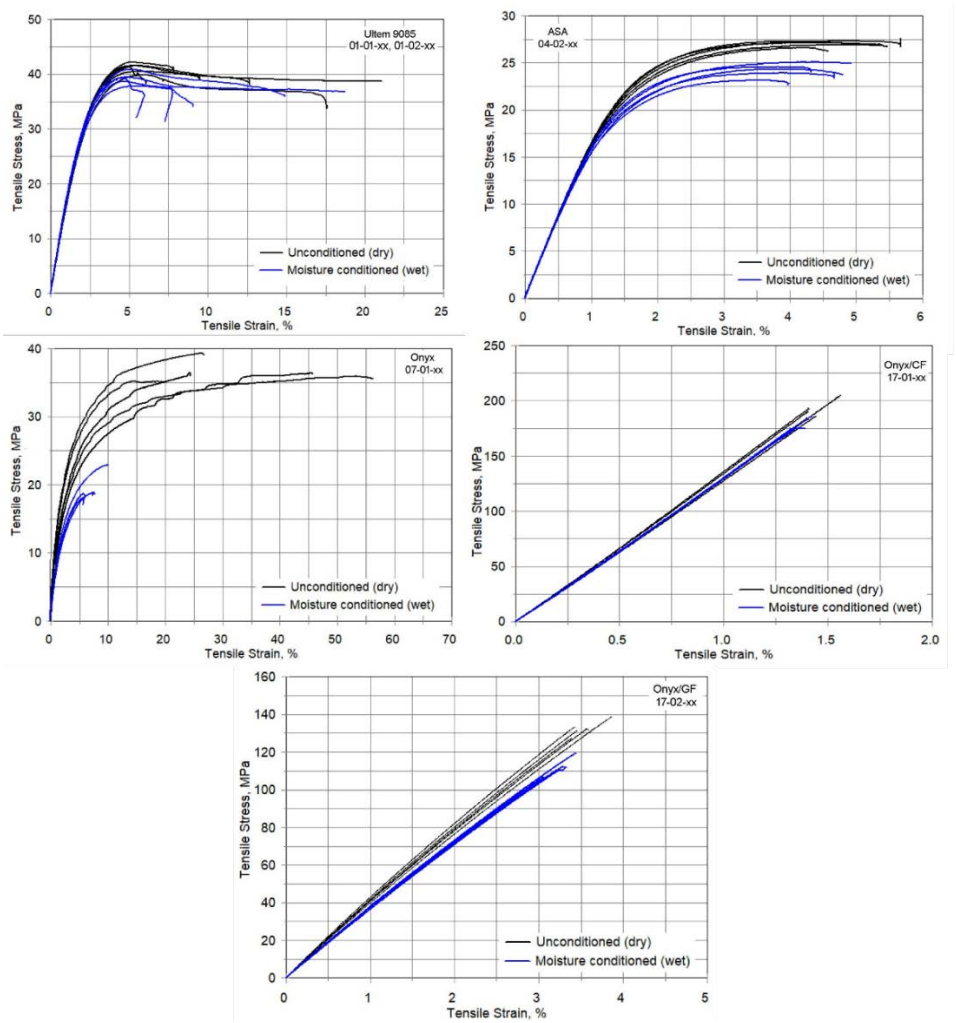

Figure 19. Stress-strain curves for the tensile specimens tested

Images from Daniel Samborsky, MSU. MPa = megapascal; CF = carbon fiber; GF = glass fiber.

4 Composite Reinforcements

Designing and manufacturing MRE components that are capable of withstanding continuous and cyclical loads from the ocean's waves and tidal currents is challenging. Structures tend to be highly loaded, so the materials used require exceptional mechanical properties. Typical 3D-printed polymers do not meet these requirements, and many efforts are being made to enhance their mechanical properties, e.g., the use of chopped-fiber reinforcements, such as chopped-carbon-fiber-filled acrylonitrile butadiene styrene, which is often used in large-format FDM printing (Post et al. 2017b), or the chopped-carbon-fiber-filled nylon (Onyx) that was tested in section 3. This approach mildly improves the thermal and mechanical properties of the polymers but is still not sufficient for MRE structural applications.

Continuous-fiber-reinforced AM technology is also making significant progress. Printing systems are being developed (and are even commercially available) with the capability of integrating continuous glass, carbon, or aramid fibers into polymer FDM prints. One example is the Markforged continuous-fiber-reinforced materials explored in section 3; however, testing showed that fiber volume fractions greater than 10%–15% could not be achieved without significant warping of the print. Additionally, the testing in section 3 highlighted poor interlaminar strengths. Ideally, fiber volume fractions should be in the range of 40%–60% to allow the mechanical properties from continuous-fiber AM to be competitive with those of conventional FRP manufacturing processes.

Other robotic processes are being developed, which are similar to automated fiber placement or filament winding but use ultraviolet-curable thermoset polymers, allowing the continuous fiber/polymer combination to be compacted and cured simultaneously as the print head moves (Ibitoye and Radford 2024). This development results in an AM technology that is capable of manufacturing high-fiber-volume-fraction, continuous FRPs into complex geometries with no tooling (or mold) requirements. This technology appears to be very promising but is still in its early research stages and not yet available at the scale required for the MRE industry.

With the current state of commercially available AM technology, simpler, more cost-effective approaches may either be to utilize AM for producing composite molds or using it to produce bulk shapes of components and then adding composite reinforcements using conventional composite manufacturing processes. Tooling costs for composite manufacturing can be prohibitive to small MRE developers, especially when prototyping and iterating on components designs and testing. The early phases of AM research in this project explored the potential for combining additive and composite manufacturing processes to optimize them for MRE components and addressed some of the associated material challenges.

4.1 Composite Manufacturing Case Study

AM has often been used to produce molds for manufacturing composite components (Li et al. 2015). Generally, these molds are contoured to the outer surface of the composite component, which makes them ideal for hydrodynamic surfaces. One of the main disadvantages is that it is impractical for a single mold to be used for a fully closed shape. For example, the high-pressure and low-pressure surfaces of a tidal turbine blade are typically manufactured as two separate shells and then adhesively bonded together afterwards. This method adds to the expense and

complexity of the process, as well as the potential for manufacturing defects, especially those found in adhesive bond lines.

In some of our research, we explored the potential of polymer additive manufacturing to produce parts that serve not only as an internal mold for the composite manufacturing but also as part of the final load-bearing structure. We also explored the unique design space that AM offers and used it to minimize the number of manufacturing steps required to produce the final component. In this instance, we used a tidal turbine blade section as a manufacturing case study. The traditional blade section would have been manufactured from three components—a high-pressure shell, a low-pressure shell, and a shear web—adhesively bonded together, each requiring their own mold. Instead, we were able to manufacture the blade section using a single-shot vacuum-assisted resin infusion process for the composite reinforcement. Additionally, root fasteners and the resin infusion lines were integrated into the single-shot infusion process. Figure 20 shows a comparison between the steps for the traditional manufacturing procedure and those for the newly developed additive/composite manufacturing approach, for both mold manufacturing and the final composite manufacturing. Figure 21 shows the final mold design, and Figure 22 shows the final part and manufacturing details. More images and description of the manufacturing process can be found in Murdy et al. (2021).

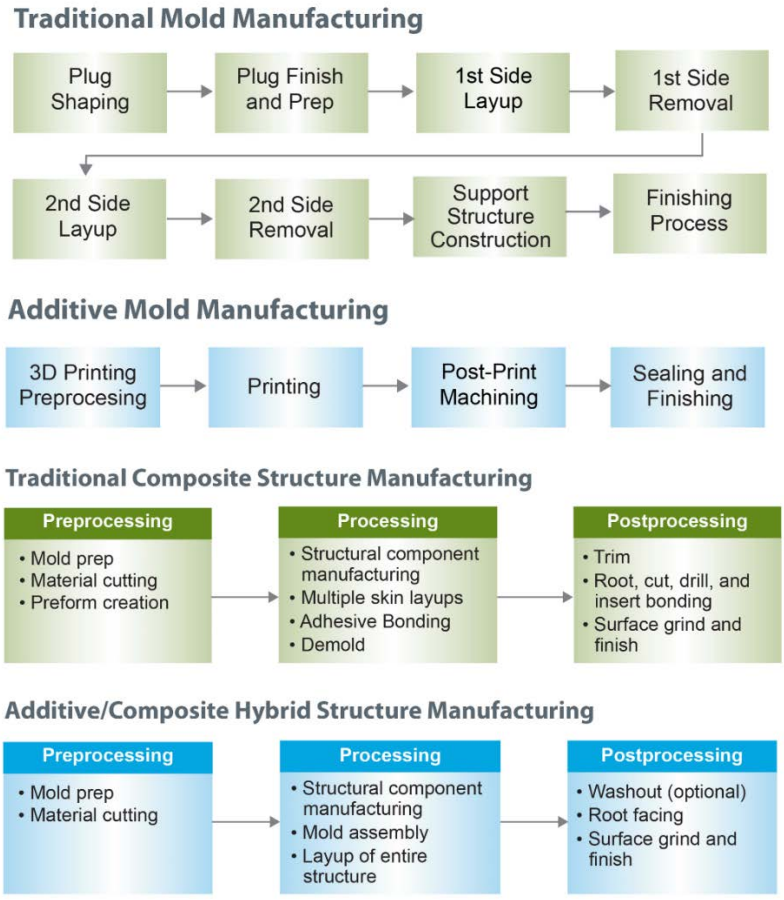

Figure 20. A comparison of mold and composite manufacturing steps for conventional manufacturing and the investigated additive/composite approach

Source: Murdy et al. (2021)

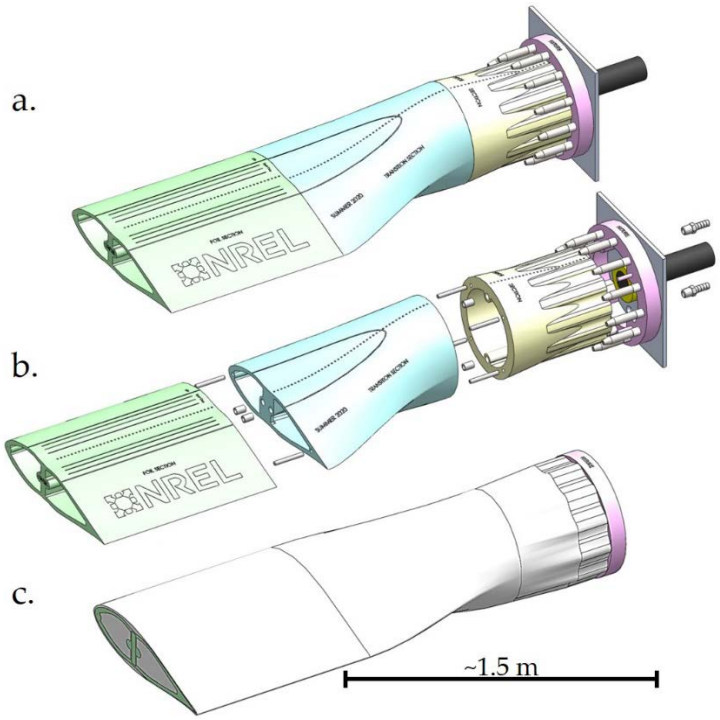

Figure 21. Computer-aided design drawings showing the AM design: (a) the assembled AM mold, (b) an exploded view of the AM mold, and (c) the AM mold with a composite overlay

Source: Murdy et al. (2021). m = meter.

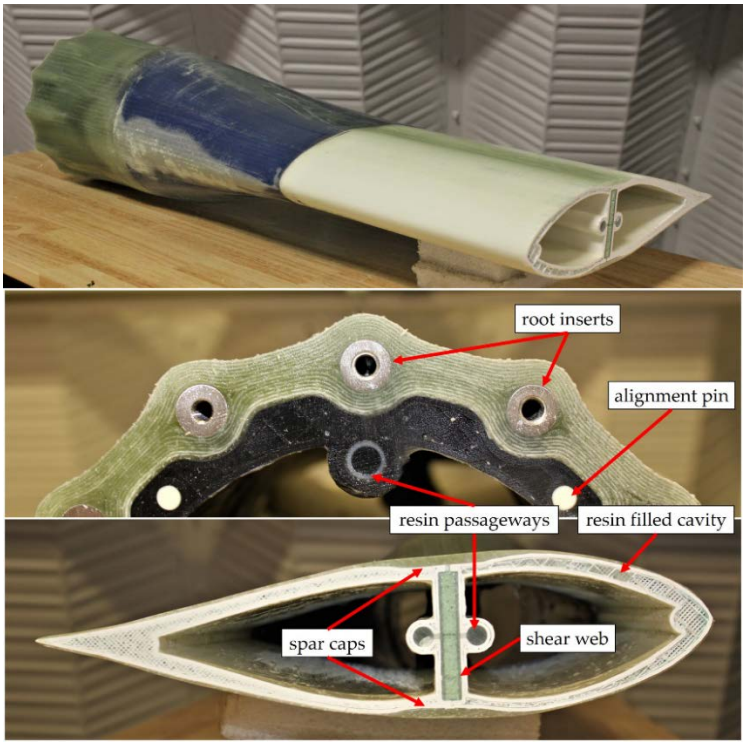

Figure 22. The completed blade section (top), root details and co-infused root fasteners (middle), and cross-section details (bottom)

Source: Murdy et al. (2021)

Overall, the final manufacturing of the blade section was very successful and proved to be very efficient. The component appeared to be high quality and met the final geometry requirements. Despite this, two key issues were highlighted during the manufacturing process:

1. The porous nature of the FDM print led to excess resin being infused into the cavities of the mold. In fact, almost double the amount of resin that was required for the composite was used during the infusion, despite efforts to seal the mold with epoxy prior to the resin infusion. This issue is somewhat explored in section 6.2.
2. The final adhesion between the composite reinforcement and the 3D-printed parts was insufficient. It was noted that the composite reinforcement debonded from the 3D-printed parts when removing the vacuum bag and peel ply after curing. A good bond between the 3D-printed part and the composite reinforcement is critical if loads are to be transferred between them. Further investigation of this issue is outlined in section 4.2.

We anticipate that this approach to composite manufacturing could be more cost-effective and reduce overall lead times, but further research is required to properly assess the advantages. This was only a manufacturing study, and no structural optimization was conducted. Structural optimization would be required to minimize the materials costs. This would then feed into technoeconomic analyses, which would be used to understand the cost differences between conventional composite manufacturing and the combined additive/composite approach. The results of these analyses would help us understand which approach is most cost-effective for a given part size and quantity.

4.2 Adhesion and Surface Preparation

In the manufacturing study outlined above, we observed that the composite reinforcement adhered poorly to the 3D-printed components. Therefore, a study was designed to investigate the effects of 3D-printed materials, composite reinforcement matrix materials, and surface preparation on the adhesion of composite reinforcements on polymer AM components. Because this application is relatively niche, little prior research has been performed to assess this problem specifically for AM polymers. Therefore, a unique approach was taken to design test specimens to evaluate their adhesive shear strength. Two 3D-printed polymers were tested: ASA and Ultem 9085. The composite reinforcements tested were fiberglass-reinforced epoxy (Westlake RIMR 035c/RIMH 1366) and fiberglass-reinforced Elium 188-O—a liquid-infusible thermoplastic resin system. Three surface preparation techniques were investigated, mainly based on typical bonding procedures:

1. Sanding with 80-grit sandpaper and wiping clean with isopropyl alcohol (IPA)
2. Vapor smoothing with acetone (Singh et al. 2017), then sanding with 80-grit sandpaper and wiping clean with IPA (ASA only)
3. Sanding with 80-grit sandpaper, wiping clean with IPA, coating and sealing with West System's 105 epoxy resin, sanding again with 80-grit sandpaper, and wiping clean once more with IPA.

Table 6 shows the 3D-printed materials, composite reinforcement matrix materials, and surface preparation techniques that were evaluated.

Table 6. The 3D-printed polymers, composite reinforcement matrices, and surface preparation techniques used to evaluate composite reinforcement adhesion

3D-Printed Polymer	Composite Matrix Material	Surface Preparation
ASA	Westlake RIMR 035c/RIMH 1366	Sand and IPA wipe
		Vapor smoothing, sand, and IPA wipe
		Sand, epoxy coating, sand, and IPA wipe
	Elium 188-O	Sand and IPA wipe
		Vapor smoothing, sand, and IPA wipe
		Sand, epoxy coating, sand, and IPA wipe
Ultem 9085	Westlake RIMR 035c/RIMH 1366	Sand and IPA wipe
		Sand, epoxy coating, sand, and IPA wipe
	Elium 188-O	Sand and IPA wipe
		Sand, epoxy coating, sand, and IPA wipe

ASTM D5868 Standard Test Method for Lap Shear Adhesion for Fiber-Reinforced Plastic Bonding was used as a reference for this study. Specimens were manufactured such that adhesive shear between the composite overlay and AM polymer would be tested over a surface area of 25 × 25 mm. To do this, sandwich panels were laid up using two plies of unidirectional glass fibers for the facesheets and 3-mm-thick AM polymer sheets as the core material. Once the surface preparation was complete, Teflon tape was strategically applied to the surfaces of the 3D-printed polymer panels to create the 25-mm adhesive bond line. The sandwich panels were then filled with resin using vacuum-assisted resin infusion (Figure 23). Multiple 3D-printed sandwich panels were manufactured in one resin infusion. Once cured, the resulting panel was then cut into the individual sandwich panels. Each individual sandwich panel was then processed in a CNC mill. The mill was programmed to cut to specific depths along the length of the Teflon-taped lines. The Teflon tape then allowed for the removal of the excess composite facesheets and 3D-printed panel sections. This removal resulted in the final lap shear test specimen geometries with integrated end taps to ensure alignment for mechanical testing (Figure 24).

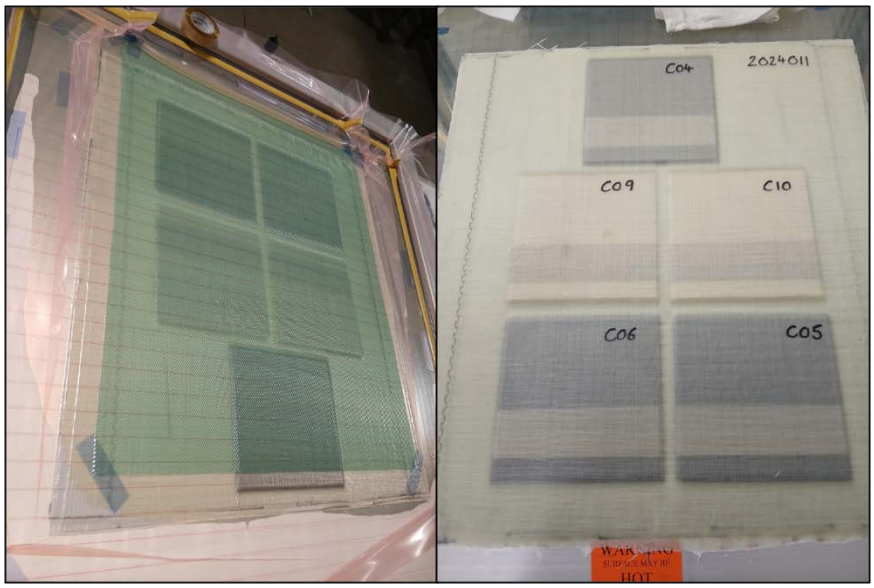

Figure 23. Multiple 3D-printed polymer/composite reinforcement panels during the vacuum-assisted resin infusion process (left), and a cured panel with the Teflon tape visible on the 3D-printed polymer surfaces (right)

Photos by Paul Murdy, NREL

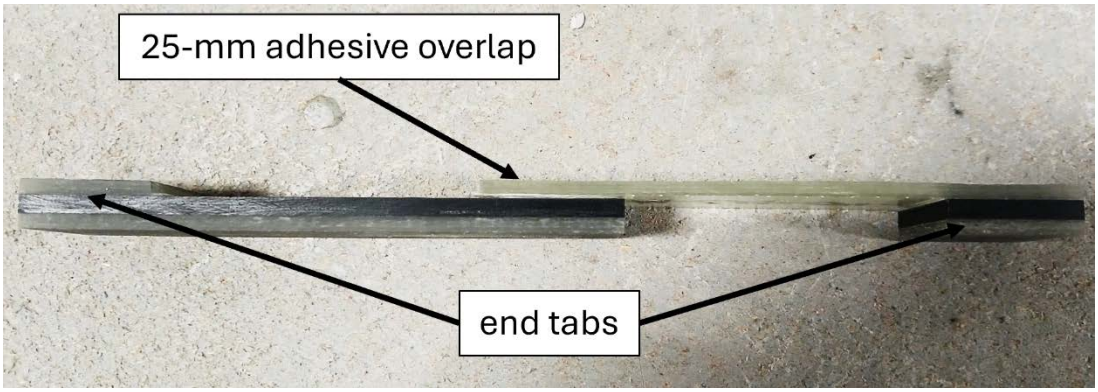

Figure 24. A final 3D-printed polymer/lap shear specimen after CNC milling and cutting to the correct width

Photo by Paul Murdy, NREL

Once cut, the lap shear area of every specimen was measured individually. Specimens were tested in tension in an MTS Systems Acumen 12-kilonewton servoelectric load frame with pneumatic grips at a rate of 1.3 mm/min. The maximum force at specimen failure was recorded and used to determine the lap shear strength of each specimen. The lap shear strength results are presented in Figure 25. Overall, it appears that the Elium matrix material consistently adhered well to the ASA and Ultem 9085 3D-printed polymers for all surface preparation conditions. Many of the specimens failed within the composite (Figure 26), indicating that the strength of the bond between the 3D-printed polymer and the composite reinforcement exceeded that of the composite reinforcement interlaminar shear strength. In comparison, the Westlake epoxy matrix composite did not adhere as well to the ASA 3D-printed material. Most of the failure modes observed were fully adhesive between the composite reinforcement and the polymer (Figure 26). Of the ASA specimens tested, the ones that were coated with epoxy prior to the resin infusion

process adhered the best to the glass/epoxy composite. The glass/epoxy-reinforced Ultem 9085 performed better. Again, the epoxy coating surface treatment promoted better adhesion than simple sanding and an IPA wipe.

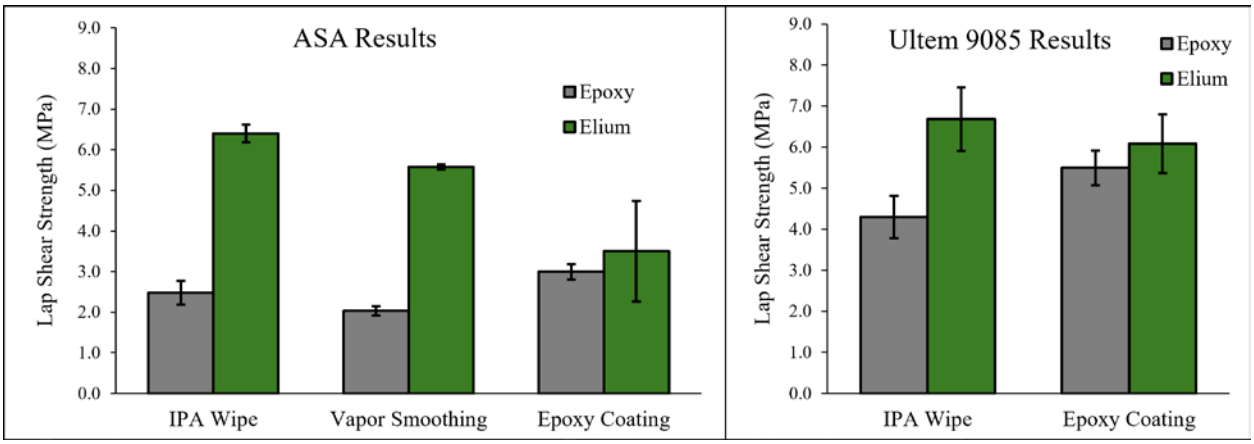

Figure 25. Comparisons of the composite reinforcement lap shear results for the ASA (left) and Ultem 9085 (right) 3D-printed polymers (error bars represent standard deviations)

Images by Paul Murdy, NREL. MPa = megapascal.

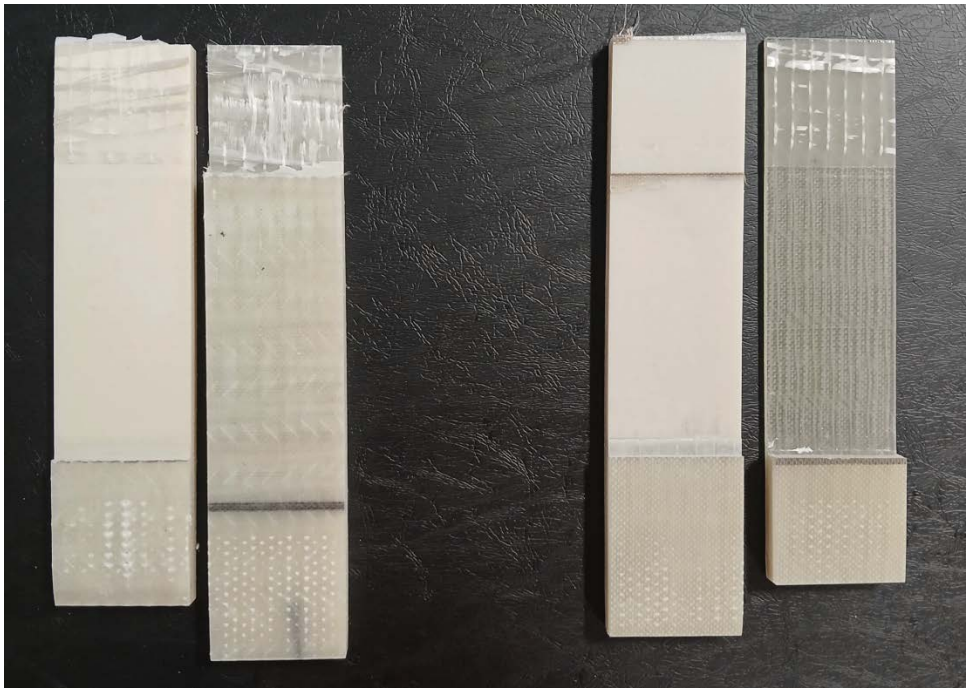

Figure 26. A comparison of composite reinforcement failures observed when testing the glass/Elium composite reinforcements (left) with the fully adhesive/interfacial failure observed for the glass/epoxy composite reinforcements (right)

Photo by Paul Murdy, NREL

Overall, this study has outlined a unique approach to evaluating the adhesion of FRP reinforcements on 3D-printed polymers. It has shown that adhesive shear strengths can vary considerably with the FRP matrix materials, 3D-printed polymers, and surface preparation techniques used. The results suggest that 3D-printed thermoplastic polymers may adhere better

to thermoplastic matrix composites like Elium, although this does not explain how the Elium also performed well with the epoxy-coated ASA and Ultem 9085. Future research could evaluate more thermoplastic matrix materials to determine if this suggestion is true. Ultimately, these results can be used to guide 3D-printed and composite material selection, but these results should not be used for design purposes.

5 Instrumentation Adhesion

Section 4 highlighted some of the issues experienced when trying to adhere composite reinforcements to 3D-printed polymer substrates. Section 3.2 also noted issues with bonding strain gages to the 3D-printed polymers that were mechanically characterized, particularly Ultem 9085. Strain gages and other instrumentation, such as accelerometers, temperature sensors, and load cells, can be critical for experimental testing and load measurements. Ensuring that sensors are bonded correctly is of great importance to guarantee good quality data are acquired.

In this section, we focused on adhesive selection for strain gages. For this study, we investigated two common off-the-shelf strain gage adhesives from Micro-Measurements:

1. M-Bond 200—an instant-curing cyanoacrylate
2. M-Bond AE-10—a room-temperature-cure two-part epoxy system.

Both adhesives were tested on ASA and Ultem 9085 substrates.

Specimens were manufactured and tested following ASTM D3163 Standard Test Method for Determining Strength of Adhesively Bonded Rigid Plastic Lap Shear Joints in Shear by Tension Loading. Lap shear specimens were manufactured using panels of 175 × 100 × 3.3 mm, which were printed on a Stratasys FDM printer. For each test condition, two panels were bonded together with a 25-mm overlap.

For the adhesive bonding, Micro-Measurements' recommendations were followed:

1. Bonding surfaces were cleaned and degreased using IPA
2. Bonding surfaces were sanded with silicon carbide paper and M-Prep Conditioner A (a mild phosphoric acid)
3. Surfaces were sanded with silicon carbide paper and M-Prep Neutralizer 5A (an ammonia-based liquid used to neutralize any reaction introduced by the conditioner)
4. Bonding surfaces were cleaned and dried
5. Adhesive was applied to the bonding surfaces
    A. For the M-Bond 200, the supplied catalyst was applied to one surface, and a thin layer of adhesive to the other
    B. For the M-Bond AE-10, the resin and hardener were mixed for 5 min at the correct ratio, and then a thin layer was applied to one bonding surface
6. The two panels were then clamped together with the 25-mm overlap and left to cure at room temperature
    A. A total of 5 min for the M-Bond 200
    B. A total of 24 hours for the M-Bond AE-10
7. End tabs with a width of 25 mm were bonded to the ends of the panels using Loctite 5-min epoxy

The 25-mm-wide specimens were cut from the resulting panels. Figure 27 shows an example of a bonded lap shear panel and a final specimen. Individual specimen overlap lengths and widths were measured to determine the cross-sectional area of the adhesive bonds.

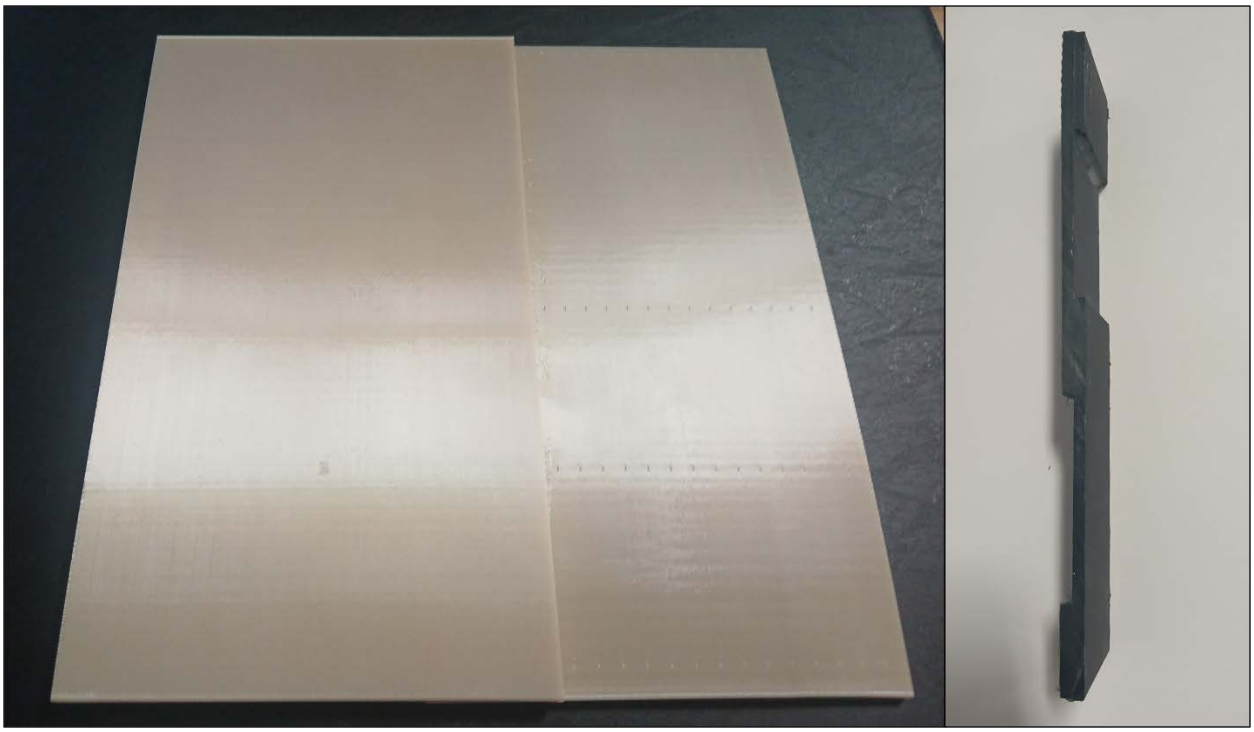

Figure 27. A bonded lap shear panel (left) and a final lap shear specimen with end tabs (right)

Photos by Paul Murdy, NREL

Specimens were tested on the MTS Systems Acumen 12-kilonewton servoelectric load frame with pneumatic wedge grips (Figure 28). All specimens were loaded to failure at a rate of 1.3 mm/min. Five to seven specimens were tested per test condition. The maximum force at failure and cross-sectional area of the adhesive bond were used to determine the ultimate lap shear strength of the various adhesive/3D-printed polymer combinations.

Figure 28. A 3D-printed polymer/strain gage adhesive lap shear specimen being tested in the load frame

Photo by Paul Murdy, NREL

Figure 29 shows a comparison of the average lap shear strengths for combinations of the two adhesives and 3D-printed polymer combinations, where the error bars represent standard deviations. For the ASA material, the results show that the average adhesive shear strengths for both adhesives were comparable. The standard deviations for the M-Bond 200 were slightly higher than those for the M-Bond AE-10, which may indicate that the M-Bond AE-10 is the more reliable choice for adhering strain gages to ASA; however, more replicate tests would be required to properly verify this. Despite this outcome, some of the specimens did not fail in pure adhesive shear (Figure 30); thus, the results may not represent the actual adhesive strength. In the future, a test should be performed with smaller overlap lengths to reduce the bonding surface area and ensure purely adhesive failures.

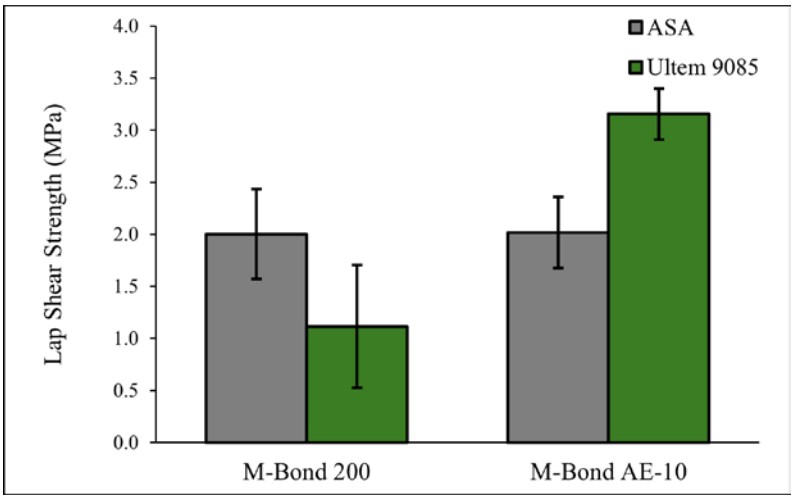

Figure 29. A comparison of adhesive shear strengths for the strain gage adhesives and 3D-printed polymers tested (error bars represent standard deviations)

Image by Paul Murdy, NREL. MPa = megapascal.

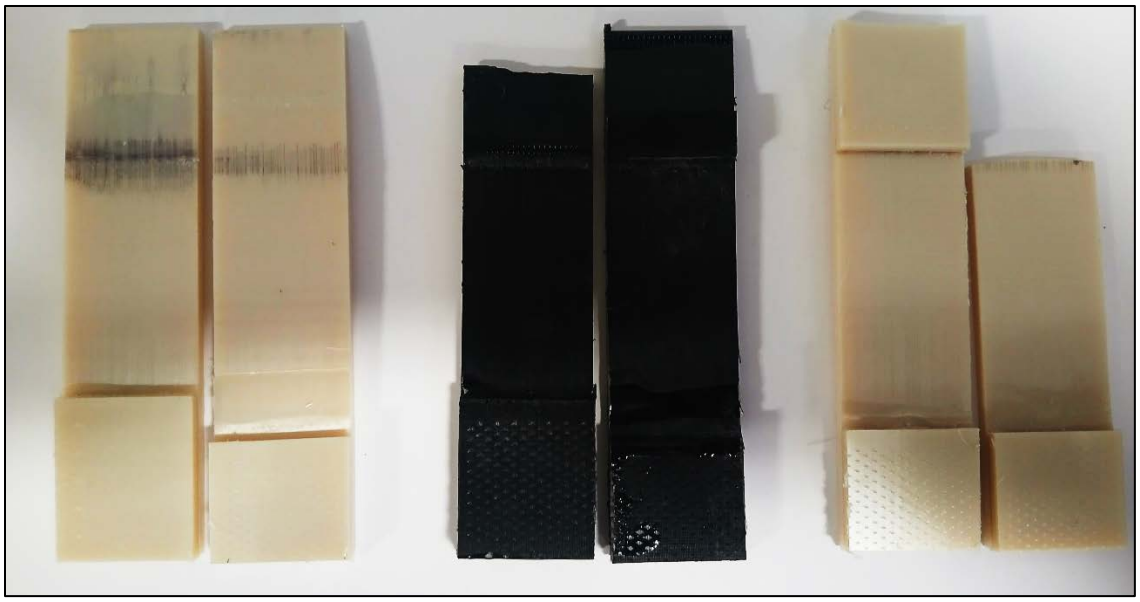

Figure 30. A comparison of failure modes for the strain gage adhesive shear specimens tested: (left) fully adhesive for the Ultem 9085/M-Bond 200 specimens, (middle) combined adhesive and tensile for several of the ASA specimens, and (right) a representative tensile failure for all the Ultem 9085/M-Bond AE-10 specimens

Photo by Paul Murdy, NREL

The results for the Ultem 9085 material show more significant differences between the adhesives tested. The adhesion of the M-Bond 200 was poor and showed large variability. This result is consistent with the strain gage failure observations noted in section 3. The M-Bond AE-10 adhered much better to the Ultem 9085. In fact, all Ultem 9085/M-Bond AE-10 specimens failed in tension rather than adhesive shear (Figure 30). Despite this, the Ultem 9085/M-Bond 200 specimens failed in adhesive shear, so it can still be concluded that the M-Bond AE-10 performed significantly better. Again, future tests should use a reduced overlap length to ensure consistent adhesive shear failures for all specimens.

Overall, this study has shown that the adhesive requirements for bonding instrumentation to 3D-printed polymer substrates can vary significantly with the polymer that is used. Generally, it appears that the epoxy-based strain gage adhesive performed better than the cyanoacrylate adhesive but takes more time to cure. For other types of instrumentation, epoxy adhesives may also be the most widely available choice for permanent installations. Also, due to the good performance of the Elium composite resin system in section 4.2, it may be worth exploring methyl-methacrylate adhesives like Plexus from ITW Performance Polymers. Ultimately, careful and clean surface preparation is key to achieving good quality adhesion.

6 Protective Coatings

The results in section 3 showed that 3D-printed polymers can degrade over extended periods of time in marine environments. Other challenges include:

- Water ingress into the cavities of FDM 3D prints due to their porous structure
- Accumulation of biofouling on the surface from microorganisms, plants, and algae present in the water
- Ultraviolet degradation.

To mitigate these issues, it may be necessary to apply coatings to 3D-printed components depending on the application. Antibiofouling paints are commonly used to prevent the accumulation of biofouling, and other coatings may be used to prevent water intrusion and ultraviolet degradation; however, common off-the-shelf products have not been evaluated for 3D-printed polymers. This section provides an initial evaluation of antibiofouling paints and potential coating solutions to prevent the ingress of water into porous 3D-printed components.

6.1 Antifouling Paints

To select the most appropriate antifouling paint for a marine environment, it is important to understand how the paint adheres to the substrate that it is to be applied to. To do this, we conducted adhesion tests per ASTM D4541 Standard Test Method for Pull-Off Strength of Coatings Using Portable Adhesion Testers. Two types of antifouling paints—Intergard 264 and SmartSol—were applied to two different 3D-printed materials—ASA and Ultem—to evaluate how well the paints adhere to the material and therefore how effective they would be if used with 3D-printed parts in a marine environment. Specimen surfaces were prepared using the paint manufacturers' recommendations. For the Intergard 264, only one coat was applied. Three coats of the SmartSol were used. Tests were performed using a DeFelsko PosiTest AT pull-off adhesion tester. Test dollies were bonded to the specimens using ResinLab EP11HT two-part epoxy; 20-mm-diameter dollies were used for the Intergard 264 specimens, and 50-mm-diameter dollies for the SmartSol specimens.

Figure 31 shows a comparison of the pull-off strength results for the two paints and two 3D-printed substrates, and Figure 32 shows examples of the failed paint specimens. A two-way analysis of variance (ANOVA) test was performed to analyze the effect of the 3D-printed base material and type of biofouling paint on the maximum pull force required to remove the paint from the material. The ANOVA test revealed that there was a statistically significant difference in the mean pull-off strength between the different base materials ($F(1) = 9.981, p = 0.004$), between the types of paint ($F(1) = 276.113, p < 0.001$), and due to the interaction of the two ($F(1) = 12.079, p = 0.002$). This test showed that the type of paint plays the most significant role in the mean pull-off strength due to the larger F-statistic calculated in the test.

These results suggest that the Intergard 264 paint is better suited for use with these 3D-printed materials. Although the testing shows that this paint adheres better to the Ultem material, it also adheres sufficiently well to the ASA material; however, the long-term performance of these two adhesions in marine environments is still unknown. Future research may focus on performing similar adhesion tests after prescribed conditioning periods in marine environments.

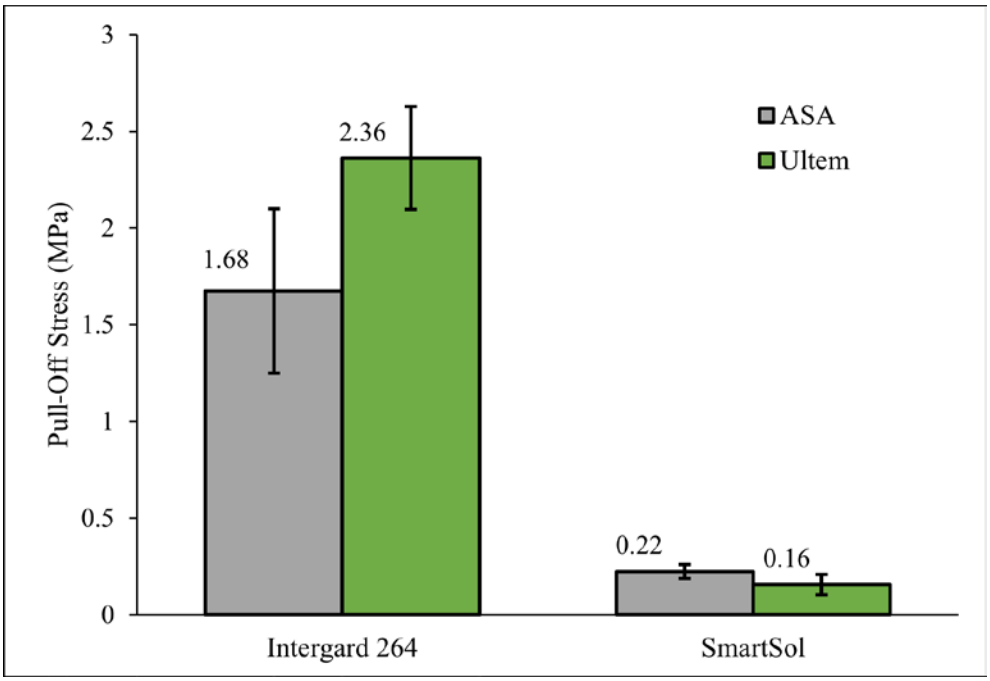

Figure 31. Biofouling coating adhesive strength (error bars represent 95% confidence interval for the mean)

Image by Charles Candon, NREL. MPa = megapascal.

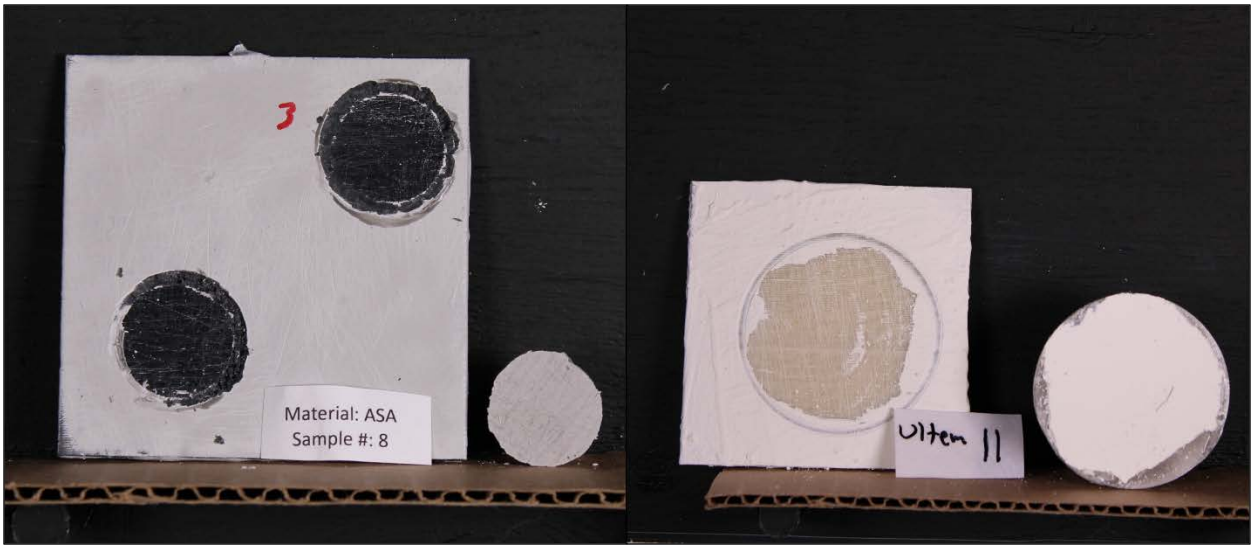

Figure 32. A comparison of failed paint specimens: (left) ASA with the Intergard 264 and 20-mm-diameter dollies and (right) Ultem 9085 with SmartSol paint and a 50-mm-diameter dolly

Photo by Joseph Daddona, PNNL

6.2 Water Ingress

To evaluate the effectiveness of coatings at preventing the ingress of water into the porous printed materials, a selection of coatings were applied to the specimens before they were submerged in water. The testing procedure is based on ASTM D570-22 Standard Test Methods for Water Absorption of Plastics. The tested samples are:

1. ASA control specimens with no coating (ASA-C)
2. ASA coated in a layer of West System's 105 epoxy resin (ASA-EP)
3. ASA coated with three layers of Minwax Helmsman Spar Polyurethane spray (ASA-PU)
4. ASA treated in acetone vapor to smooth and fuse FDM layers (ASA-VS)
5. Ultem 9085 control specimens with no coating (Ultem-C)
6. Ultem 9085 coated in a layer of West System's 105 epoxy resin (Ultem-EP)
7. Ultem 9085 coated with three layers of Minwax Helmsman Spar Polyurethane spray (Ultem-PU).

The specimens were printed with default settings on a Stratasys Fortus 400mc. For each coating type, seven specimens were prepared and tested. The specimens were 75 mm long, 25 mm wide, and 3 mm thick.

The specimens were first dried in an oven at 50°C for 24 hours. The initial mass of each specimen was recorded, and then each was submerged in distilled water at room temperature. Mass measurements were taken after 2 hours, 24 hours, 1 week, and then every 2 weeks after. Before weighing, the surface moisture was wiped from each specimen with a paper towel. Each mass was then recorded to the nearest 0.1 milligram. The results for the average percent change in mass for each specimen type are shown below in Figure 33.

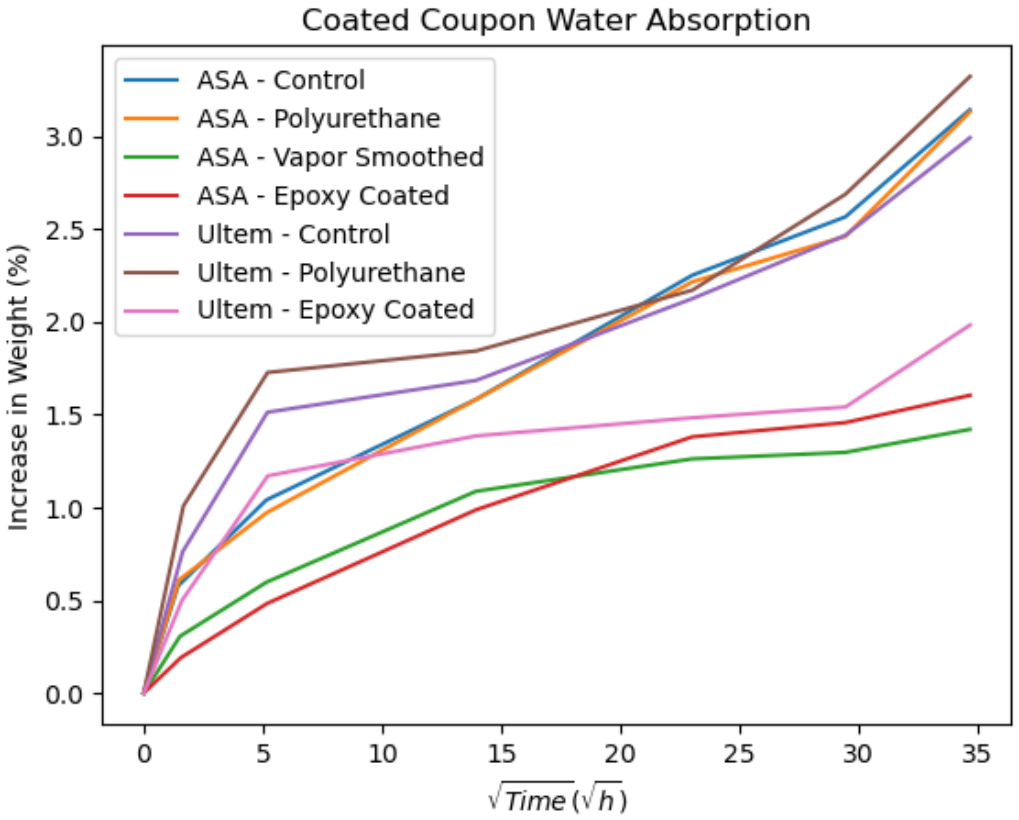

Figure 33. Water uptake of coated specimens over time

Image by Charles Candon, NREL. g = gram; h = hour.

The weight data will continue to be recorded every two weeks until a plateau is reached. Due to the time constraints in creating this report, these specimens were measured for only 7 weeks, although trends can still be observed in this time period. Because of this limited duration, the maximum mass changes (or m_∞ values) are still unknown. Mass measurements will continue to be taken until no more water is absorbed by the plastic. These results will be published at a later date.

The initial slope of the long-term immersion data is proportional to the diffusion constant of the water in this sample. This constant can be used to quantify how well the coatings prevent the ingress of water; the corresponding results are compared in Figure 34.

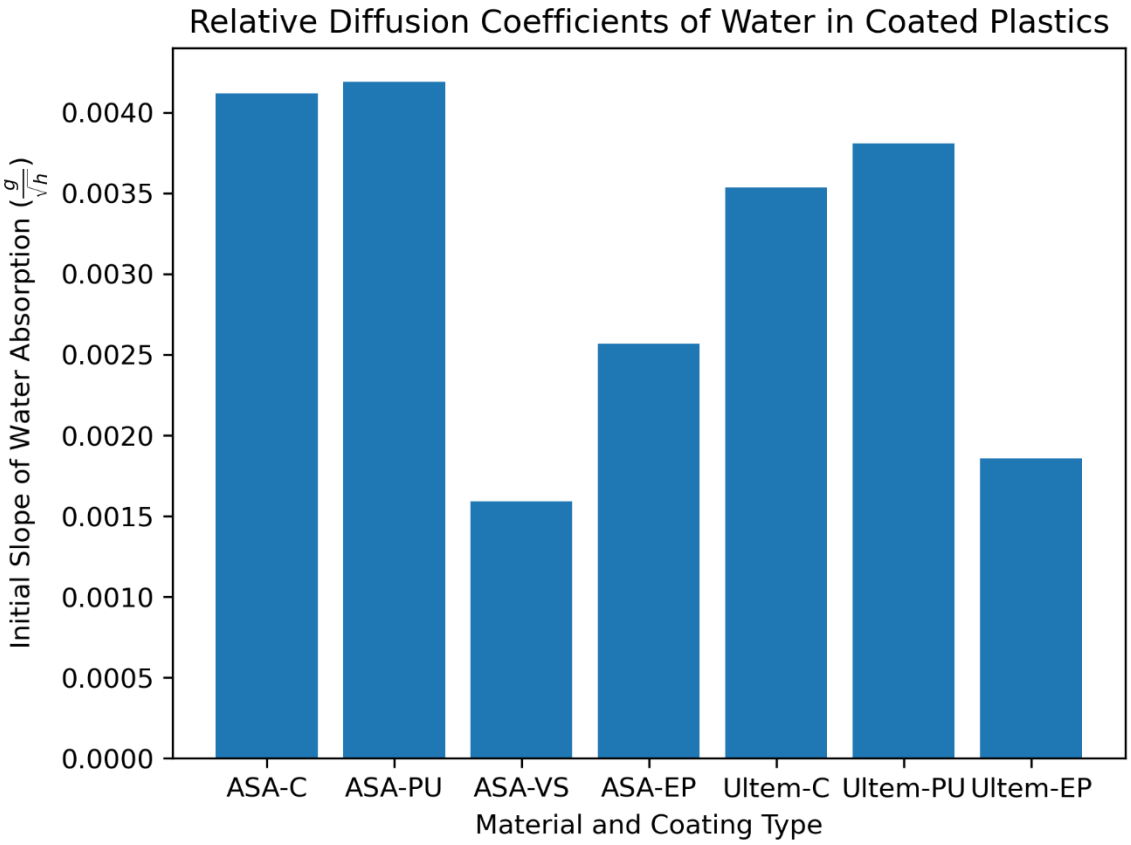

Figure 34. Relative diffusion coefficients of water in coated plastic specimens, where lower is better

Image by Charles Candon, NREL. g = gram; h = hour.

From Figure 34, we can see that the vapor-smoothed ASA, epoxy-coated ASA, and epoxy-coated Ultem were most effective at preventing water ingress. Therefore, for FDM polymer prints, it is recommended that either epoxy coatings or vapor smoothing be used. Overall, the epoxy coating was much easier to apply to the specimen surfaces. The vapor smoothing was more challenging. Timing was critical to ensure that the acetone vapors did not cause warping of the specimen geometries, while still producing a smooth and sealed surface.

7 Other Applications and Case Studies

In the previous sections, this report outlined some of the advantages and challenges associated with utilizing 3D-printing processes and polymeric materials for marine energy components and structures at various scales. The studies outlined offer only a sample of what is possible when applying 3D printing to the MRE industry. In fact, there are many other cases where 3D printing has proved to be particularly useful, as well as time- and cost-effective when applied to MRE research and development, such that it is becoming a regular tool for researchers and technology developers. This section outlines several notable case studies outside of the Advanced Materials project that found AM to be particularly beneficial, as well as highlighting their challenges and lessons learned, such that users can utilize AM as a more effective tool in future projects.

7.1 Tidal Turbine Blade Composite Mold Sections

Two-part glass-fiber-reinforced composite tidal turbine blades were designed and built at NREL as part of the development of a novel recyclable-by-design epoxy resin system (Wang et al. 2023). The blade shells were manufactured using vacuum-assisted resin infusion molding. During the fabrication of composite tidal turbine blades, a set of 3D-printed "return flanges" were used as a part of the blade tooling. A return flange is a removable piece connected to the primary mold to enable the fabrication of composite parts that have a final geometry with negative draft that would otherwise be impossible to demold. After the composite part is produced, the return flange is disconnected, which allows the composite part to be removed from the mold.

The design requirements for the return flanges were not as stringent as those for the primary molds. They did not require vacuum integrity because they were completely covered by the vacuum bag, and they have lower stiffness requirements. For this project, both the high-pressure and low-pressure blade skins were constructed on aluminum molds that had return flanges that were 3D-printed with Ultem material. Like the aluminum molds, the return flanges were treated with a Chemlease mold release system that was specific to the epoxy resin system being used. This 3D-printing approach enabled cheaper and faster tool development. The low-pressure skin primary mold, return flange, and blade skin can be seen in Figure 35.

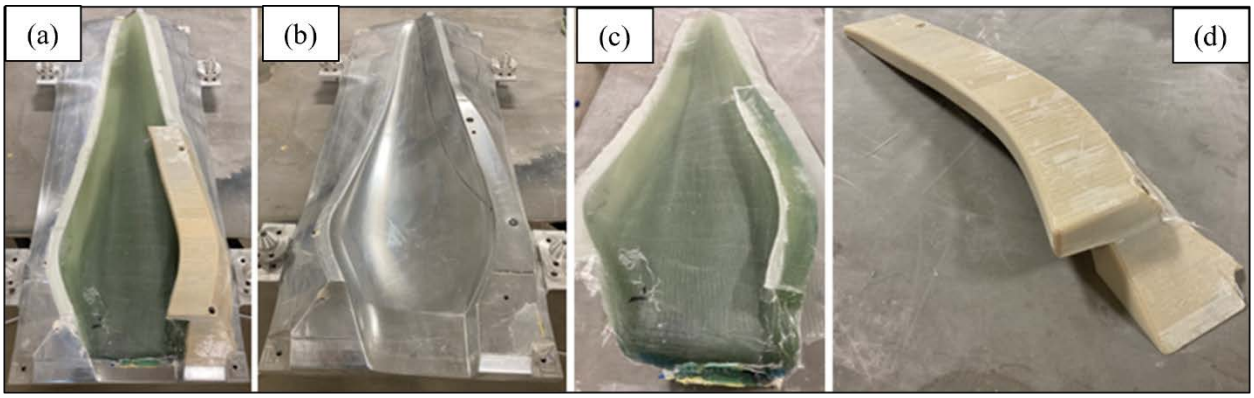

Figure 35. (a) The as-manufactured assembly containing (b) the primary mold, (c) the blade skin, and (d) the return flange

Photos by Ryan Beach, NREL

7.2 Instrumentation Splice Connections

As part of a large, in-lab, submerged bolted connection study, instrumented studs were used to measure changes in the preload of composite bolted joints over long periods of time. To do this, strain gages were embedded in the center of the studs (Figure 36), with the lead wires exiting the end of the studs. Because the studs were to be stored underwater for extended periods of time (>12 months), the splice connection between the lead wires and the wires connected to the data acquisition system needed to be protected. 3M Scotchcast electrical insulating resin is commonly used for such applications; however, the shape of the mold that comes with the kit was not suitable for this study. Instead, bespoke two-part molds were designed and 3D-printed to be clamped onto the final threaded portions of the studs so that the Scotchcast resin could be injected to encase the strain gage splice connection (Figure 36). The molds were manufactured using a Markforged Mark 2 printer with the chopped-carbon-fiber-filled nylon filament. Overall, this manufacturing process proved to be successful, as the molds could be designed and manufactured in a matter of hours, which resulted in significant cost savings. Despite this result, two design iterations were required due to larger-than-expected tolerances from the 3D-printing process.

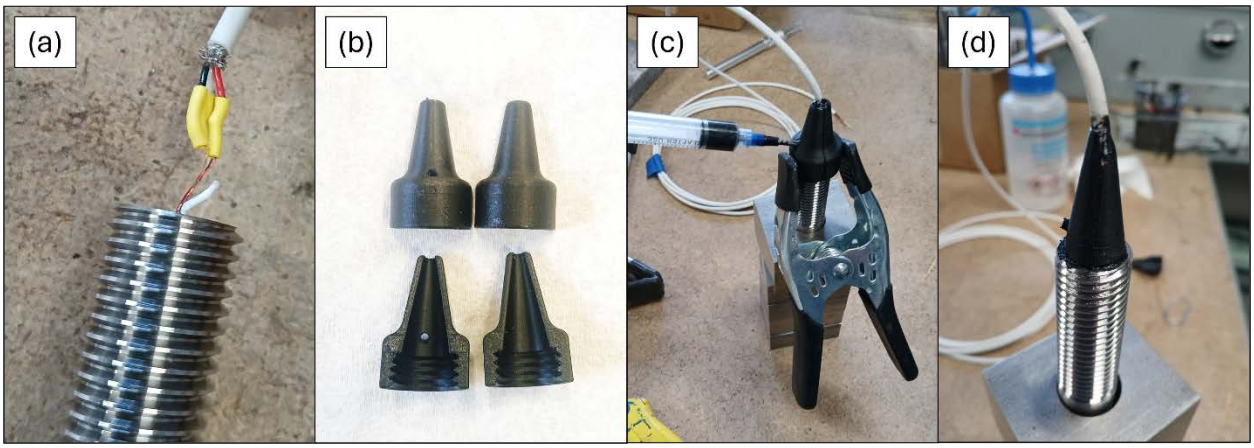

Figure 36. (a) The splice connection at the end of the instrumented studs, (b) external and internal details of the 3D-printed Scotchcast molds, (c) Scotchcast being injected into the mold, and (d) the final cured splice connection

Photos by Paul Murdy, NREL

7.3 Wave Tank Models

AM is a valuable tool for preparing scale models of devices for scaled performance validation in wave tanks. It allows for device models to be manufactured in house with minimal involvement from experienced machinists and model builders. Accurately scaled device models can be prepared in computer-aided design software and then printed and tested in a laboratory wave tank.

3D printing has been leveraged at NREL to prepare wave energy converter models for experimentation in the Sea Wave Environmental Laboratory (SWEL) wave tank. For example, a 1/100th scale model of the Reference Model 3 (RM3) wave point absorber was fabricated in house and tested at SWEL. The float structure of the RM3 model would have taken significant effort to fabricate using traditional methods such as CNC machined tooling foam. As an

alternative, the float was printed as a single part with black ASA plastic on a Stratasys F370 FDM printer. The part was then coated in a layer of West System's 105 epoxy to prevent water ingress between the FDM layers. Additional parts fabricated with 3D printing are shown in Figure 37 and described in Table 7. Figure 38 shows the wave point absorber being tested in SWEL's wave tank.

Table 7. Descriptions of RM3 components that were 3D-printed

	Description	Process/Material	Key Benefit
1	12-sided float	FDM/ASA	Took advantage of the large build volume of the FDM printer
2	Motion tracker marker mount	Stereolithography (SLA)/ultraviolet-curable resin	Eliminated the need for a machined part
3	Bearing sleeve	SLA/ultraviolet-curable resin	Tight tolerances enabled by SLA printing
4	Mooring attachment plate	FDM/continuous-carbon-fiber-reinforced Onyx	Continuous fiber provides increased strength and stiffness for the mooring connection points
5	Bottom gasket seal	SLA/ultraviolet-curable resin	SLA is inherently sealed from water ingress, and the small layer height allows for a smooth surface and tight seal with a gasket
6	Load cell adaptor	FDM/PLA	Eliminated the need for a machined part
7	Tube adaptor	SLA/ultraviolet-curable resin	Inherently sealed, tight tolerance, and optically translucent

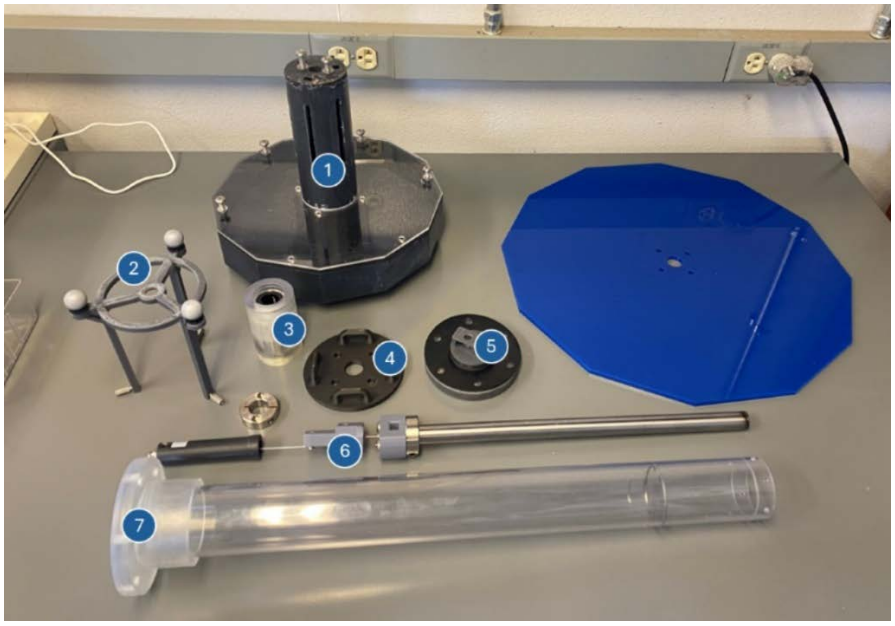

Figure 37. Disassembled RM3 model with 3D-printed components labeled per Table 7

Photo by Charles Candon, NREL

Figure 38. 3D-printed RM3 model being tested at NREL's Sea Wave Environmental Laboratory

Photo by Charles Candon, NREL

While 3D printing offers significant benefits for rapid prototyping, it also presents some limitations. The largest single part that can be fabricated with current NREL printers is 14 in. × 10 in. × 14 in. Larger parts would need to be printed in multiple parts then combined with adhesives. This adds additional manufacturing steps and may result in less dimensionally accurate parts. Additionally, FDM-printed parts are inherently porous and will require additional coatings to be applied to make parts water tight. SLA-printed parts do not have this problem but are more limited in size and lack the option to add dissolvable support material.

7.4 Distributed Embedded Energy Converter Technologies

Distributed embedded energy converter technologies (or DEEC-Tec) are an emerging space in which many small DEECs are combined to produce "DEEC-Tec metamaterials" to harvest energy. DEECs can take many forms to convert motion into useable energy—e.g., variable capacitance (dielectric elastomers), piezoelectric, triboelectric, microfluid, and microelectromechanical systems. This technology space is currently being explored for flexible wave energy converters (Mendoza, Boren, and Niffenegger 2023). Because it is a nascent yet very broad research area, there is a need for rapidly assessing, prototyping, and characterizing various concepts and geometries. The DEEC-Tec project team at NREL has seen significant benefits from applying AM to their research.

One notable use case has been the development of a bespoke low-force tensile test machine to characterize hyperelastic materials and measure their variable capacitance responses (Chamot, Niffenegger, and Boren 2024). Figure 39 shows a diagram of the test rig that has been developed. Most of the components on the machine were manufactured using FDM 3D printing, which allowed for fast and cost-effective development and iteration of the machine components.

This process was particularly useful for the grips for the clamping test specimens. The clamping force required for the elastomeric specimens was highly dependent on the texture of the grip surfaces. Therefore, several grip surfaces needed to be tested. The Markforged Mark 2 printer was used, which had sufficient resolution to manufacture grips with serrated textures on the surface—a feature that would likely require specialized techniques if CNC machining was used instead.

Additionally, 3D printing was very useful for implementing machine safeguarding for various belts and pinion gears that were used in the construction of the bespoke test systems. Nevertheless, some challenges were encountered, particularly regarding the stiffness of the components and ease of hardware integration. As mentioned in section 4, the stiffness and strength of typically available 3D-printed polymers are not comparable between composites and metals and thus serve as a barrier to the broader implementation of many AM technologies. Also, even with very precise FDM 3D printers, manufacturing tolerances are dictated by bead widths, which can make implementing hardware, such as screws and bolts, difficult.

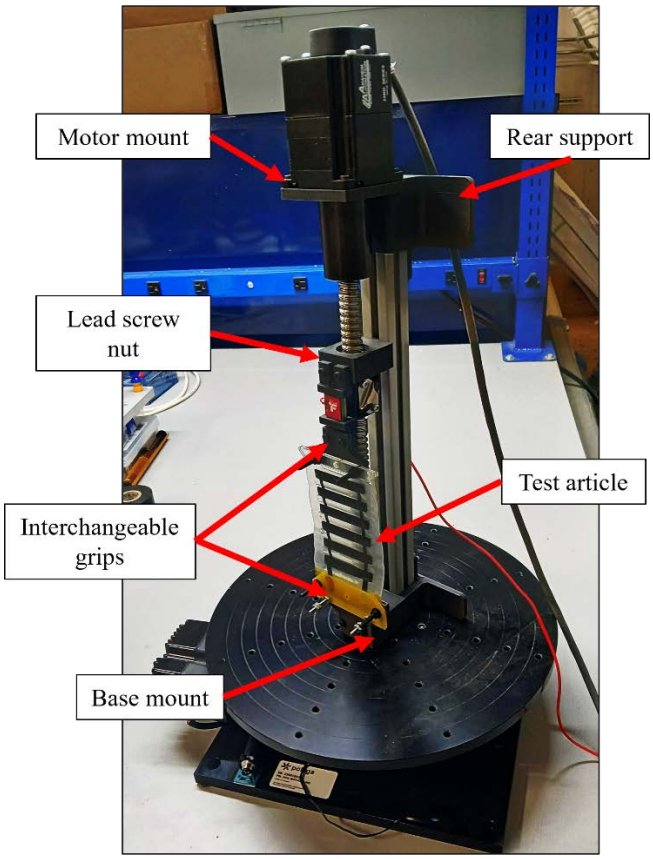

Figure 39. A diagram of the bespoke low-force tensile test machine for hyperelastic materials developed by NREL's DEEC-Tec team, highlighting the 3D-printed components

Photo by Paul Murdy, NREL

Another example is the DEEC-Tec team's use of stereolithography (SLA) printing to produce the housings for magnetic-induction-based wave energy converters to be tested in a wave tank (Figure 40). SLA printed uses ultraviolet-curable resins to produce high-resolution parts layer by layer. While FDM-printed parts are typically porous, SLA parts can be watertight because the

process repeatedly cures thermoset resin layer by layer rather than by stacking thick beads of molten thermoplastic on top of each other. The housings for the generators were 3D-printed rather than casting them in silicone, as they had done previously. This choice allowed them to access the electronics during or after testing to make modifications without having to manufacture new components. Additionally, the SLA printing approach permitted more complex feature integration with tighter tolerances in the internal geometry that would be difficult to achieve with CNC machining or even injection molding.

Some limitations were found with the SLA printing process. SLA printing is generally known to be less scalable than FDM, so build volumes are limited with commercially available SLA printers. Also, the team found the thermoset polymer housings were quite brittle, as can be typical with thermosetting polymers. Tougher, more durable SLA resins are commercially available but have not yet been tested by the team.

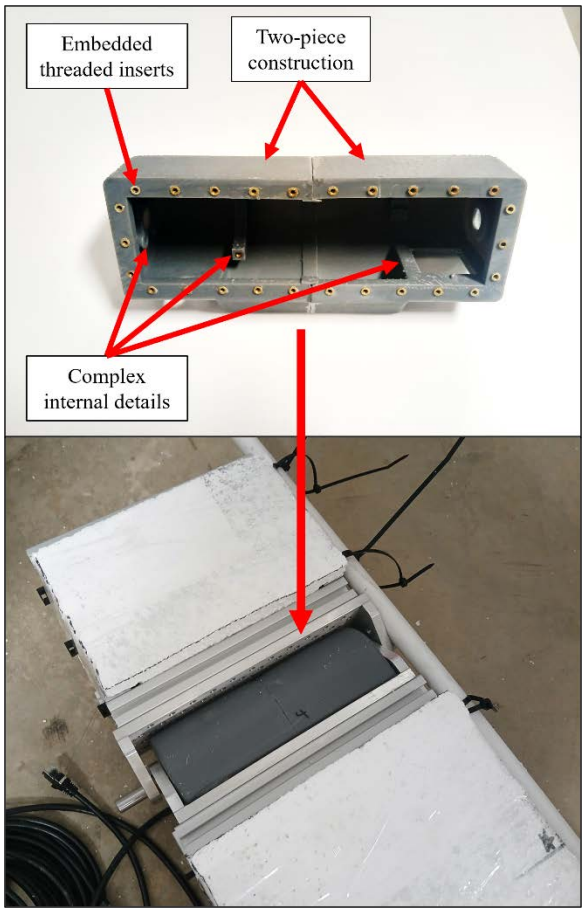

Figure 40. A diagram of the housing for a magnetic-induction DEEC produced using SLA printing (top) and the housing integrated into a wave energy converter for wave tank testing (bottom)

Photos by Paul Murdy, NREL

7.5 Instrumentation for Deployments

In the construction of data acquisition systems for marine energy deployments, 3D printing is commonly used for mounting components inside enclosures. A prime example of this is NREL's black box system (Figure 41). The black box is a miniature data acquisition system in a

cylindrical aluminum enclosure. To mount components inside this unique enclosure, a Stratasys F370 printer was used to fabricate an electronics shelf and battery housing from ASA plastic. 3D printing of these components streamlined the prototyping and fabrication processes.

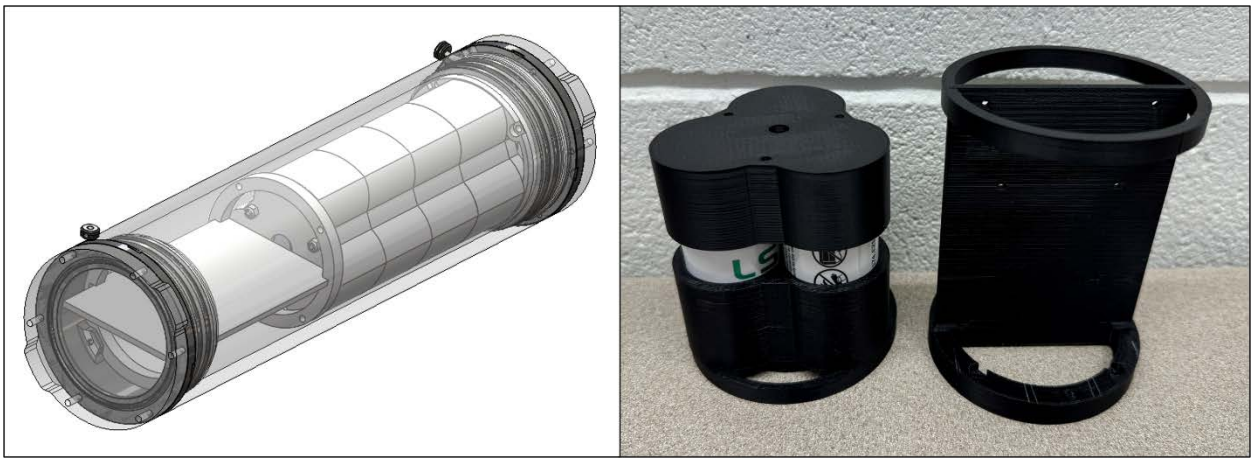

Figure 41. CAD drawing of the black box data acquisition system featuring 3D-printed electronics mounting and battery housing (left) and a photo of the 3D-printed components (right)

Images by Charles Candon, NREL

7.6 Stainless-Steel Tidal Turbine Spar

Although this report has primarily focused on polymeric AM techniques, this final case study relates to metal AM to demonstrate that the MRE research community is beginning to explore the potential of scalable metal AM processes. In this case study, the research team designed and manufactured a 1-m-long tidal turbine blade spar from 316L stainless steel with a Meltio laser metal deposition AM system (Gonzalez-Montijo et al. 2023). The spar incorporated unique internal geometries, as well as taper, twist and wall thickness tailoring along the length (Figure 42). It would be difficult to manufacture this complex geometry as a single piece with conventional subtractive metal manufacturing processes due to the closed geometry. After manufacturing, the team found several defects in the form of surface roughness and significant warpage at the thick root buildup. They suspected that the spar contained a significant amount of residual thermal stresses. Because of this issue, postprocessing was required to smooth the external surface and integrate the root connections points. It may be possible to mitigate these defects in future iterations with refinements to the printing strategy and root geometry; however, this example shows that the laser metal deposition process is much more complex than the other more user-friendly processes outlined in the rest of this report.

Figure 42. A photo of the 316L stainless steel turbine blade spar mounted to the structural test stand

Photo by Paul Murdy, NREL

Once the final machining was complete, the spar was subjected to several structural test load cases. First, static testing was conducted up to 125% of the spar's design load. Then, fatigue testing was conducted for 250,000 cycles at 100% of the spar's design load, followed by 250,000 cycles at 125% of the design load. Finally, incrementally increasing static loads were applied, up to 275% of the original design load. Although, the spar did not fail catastrophically, the displacement and strain data did show small amounts of yielding of the steel—on the order of 1 mm of irrecoverable displacement at the tip. Nonetheless, this showed that the design could withstand repeated loading and overloading in harsh marine environments. Also, the design could be further refined and optimized by reducing wall and root thicknesses to reduce material usage and overall material costs.

8 Conclusions and Future Research

This report has outlined a broad variety of AM polymer research that was performed as part of WPTO's Marine Energy Advanced Materials project over the past 4 years and how common AM material and manufacturing challenges have been addressed in that time—from material and process selection to mechanical characterization, adhesion of composite reinforcements and instrumentation, and protective coatings for various laboratory and marine underwater environments. Although the data are limited to a small selection of materials and processes, we have done our best to recommend best practices for characterizing materials for current and future AM processes and materials. Ultimately, the results showed that mechanical properties and material compatibility can vary considerably between materials and processes. Therefore, the best way to mitigate risks when introducing AM polymers to new components is through rigorous characterization to qualify them for use in marine environments. This approach holds true for any new material or manufacturing process being used for a new application or environment.

Because of the materials science focus of this report, one thing that has not been explored in depth beyond the case studies in section 7 is the unique design space that AM offers. AM allows the designer to incorporate complex internal geometries into component designs, which can reduce the number of components required, as well as optimize the design to reduce material usage and final material costs. To date, the techno-economics of AM processes and materials in the MRE industry have not been fully explored to properly understand the value that AM could bring to the industry and on what order of part quantities and scales would AM be the most cost-effective option. Also, the idea of site-specific tailoring for MRE technologies through AM has often been pitched as a potential benefit. AM offers the opportunity to easily modify hydrodynamic designs depending on site-specific flow conditions with minimal changes to tooling in the manufacturing process. To fully understand the nuances of these aspects, a more holistic approach to the techno-economic analysis would be required, i.e., an approach that incorporates the design and manufacturing process from start to finish—process and material selection, design and process optimization, and final manufacturing and processing. Only then can we determine what materials, processes, quantities, and scales will be optimal for AM in the MRE industry. Beyond what has been stated in the previous chapters, future research should also focus on developing this framework and continue to be adapted as both the MRE and AM industries mature and new concepts, materials, and processes are introduced.

References

Abdulsalam, M. I., and F. Presuel-Moreno. 2021. "Investigation of Crevice Corrosion of Metallic Fastened Joints in Carbon Fiber Reinforced Polymer (CFRP) Exposed to Coastal Seawater." *Anti-Corrosion Methods and Materials* 68 (3): 238–247. https://doi.org/10.1108/ACMM-11-2020-2405.

Bassett, K., R. Carriveau, and D. S. K. Ting. 2015. "3D Printed Wind Turbines Part 1: Design Considerations and Rapid Manufacture Potential." *Sustainable Energy Technologies and Assessments* 11: 186–193. https://doi.org/10.1016/j.seta.2015.01.002.

Carron, W. S., D. Snowberg, P. Murdy, and S. Hughes. 2023. *Using Large-Scale Additive Manufacturing for Wind Turbine Blade Core Structures*. Golden, CO: National Renewable Energy Laboratory. NREL/TP-5000-85673. https://doi.org/10.2172/1994799.

Chamot, S., J. Niffenegger, and B. Boren. 2024. "Characterization of Hyperelastic Tranducers - DEEC-Tec & Marine Renewable Energy." Presented at the International Conference on Ocean Energy, Melbourne, Australia, September 17–19.

Gonzalez-Montijo, M., P. Murdy, C. Candon, R. Beach, C. Nichols, and P. Barden. 2023. "Additive Manufacturing for Powering the Blue Economy Applications: A Tidal Turbine Blade Case Study." Presented at the European Wave and Tidal Energy Conference, Bilbao, Spain, September 3–7. https://doi.org/10.36688/ewtec-2023-420.

Hernandez-Sanchez, B. A., and G. T. Bonheyo. 2017. "Controlling Biofouling for Marine Hydrokinetic Technology." Presnted at the EPRI Interest Group Webcast, United States, May 9. https://www.osti.gov/biblio/1457969.

Ibitoye, F. A., and D. W. Radford. 2024. "Experimental and Statistical Study on the Effect of Process Parameters on the Quality of Continuous Fiber Composites Made via Additive Manufacturing." *Journal of Thermoplastic Composite Materials*. https://doi.org/10.1177/08927057241241504.

Jacobson, P. T., G. Hagerman, and G. Scott. 2011. *Mapping and Assessment of the United States Ocean Wave Energy Resource.* United States: Electric Power Research Institute. DOE/GO/18173-1. https://doi.org/10.2172/1060943.

Jones, K. E. S., and M. Li. 2023. "Life Cycle Assessment of Ultra-Tall Wind Turbine Towers Comparing Concrete Additive Manufacturing to Conventional Manufacturing." *Journal of Cleaner Production* 417: 137709. https://doi.org/10.1016/j.jclepro.2023.137709.

Kim, J., and B. S. Kang. 2020. "Enhancing Structural Performance of Short Fiber Reinforced Objects through Customized Tool-Path." *Applied Sciences* 10 (22): 8168. https://doi.org/10.3390/app10228168.

Li, H., G. Taylor, V. Bheemreddy, O. Iyibilgin, M. Leu, and K. Chandrashekhara. 2015. "Modeling and Characterization of Fused Deposition Modeling Tooling for Vacuum Assisted Resin Transfer Molding Process." *Additive Manufacturing* 7: 64–72. https://doi.org/10.1016/j.addma.2015.02.003.

Mandell, J. F., D. D. Samborsky, D. A. Miller, P. Agastra, and A. T. Sears. 2016. *Analysis of SNL/MSU/DOE Fatigue Database Trends for Wind Turbine Blade Materials, 2010–2015.* Albuquerque, NM: Sandia National Laboratories. SAND-2016-1441. https://doi.org/10.2172/1431256.

Mendoza, N., B. Boren, and J. Niffenegger. 2023. *Distributed Embedded Energy Converter Technologies for Marine Renewable Energy (A Technical Report).* Golden, CO: National Renewable Energy Laboratory. NREL/TP-5700-85158. https://doi.org/10.2172/1997371.

Miller, D. A., D. D. Samborsky, M. T. Stoffels, M. M. Voth, J. D. Nunemaker, K. J. Newhouse, and B. A. Hernandez-Sanchez. 2020. *Summary of Marine and Hydrokinetic (MHK) Composites Testing at Montana State University.* Albuquerque, NM: Sandia National Laboratories. SAND-2020-9562. https://doi.org/10.2172/1668132.

Murdy, P., J. Dolson, D. Miller, S. Hughes, and R. Beach. 2021. "Leveraging the Advantages of Additive Manufacturing To Produce Advanced Hybrid Composite Structures for Marine Energy Systems." *Applied Sciences* 11 (3): 1336. https://doi.org/10.3390/app11031336.

Murdy, P., S. Hughes, D. Miller, F. Presuel-Moreno, G. Bonheyo, B. Hernandez-Sanchez, and B. Gunawan. 2023a. *Subcomponent Validation of Composite Joints for the Marine Energy Advanced Materials Project.* Golden, CO: National Renewable Energy Laboratory. NREL/TP-5700-84487. https://doi.org/10.2172/1909582.

Murdy, P., S. Hughes, D. A. Miller, F. J. Presuel-Moreno, G. T. Bonheyo, B. Gunawan, and B. A. Hernandez-Sanchez. 2023b. "Static and Fatigue Characterization of Large Composite T-Bolt Connections in Marine Hygrothermal Environments." *Journal of Marine Science and Engineering* 11 (12): 2309. https://doi.org/10.3390/jmse11122309.

Murdy, P., J. O'Dell, D. Barnes, J. R. McVey, and C. Rumple. 2023. "Investigating Marine Environmental Degradation of Additive Manufacturing Materials for Renewable Energy Applications." Presented at CAMX, Atlanta, GA, October 30–November 2. https://www.nrel.gov/docs/fy23osti/86315.pdf.

Murray, R. E., A. Simms, A. Bharath, R. Beach, M. Murphy, L. Kilcher, and A. Scholbrock. 2023. "Toward the Instrumentation and Data Acquisition of a Tidal Turbine in Real Site Conditions." *Energies* 16 (3): 1255. https://doi.org/10.3390/en16031255.

Neary, V. S., M. Previsic, R. A. Jepson, M. J. Lawson, Y. H. Yu, A. E. Copping, A. A. Fontaine, K. C. Hallet, and D. K. Murray. 2014. *Methodology for Design and Economic Analysis of Marine Energy Conversion (MEC) Technologies.* Albuquerque, NM: Sandia National Larboratories. SAND-2014-9040. https://doi.org/10.13140/RG.2.2.10201.95846.

Post, B., B. Richardson, P. Lloyd, L. Love, S. Nolet, and J. Hannan. 2017a. *Additive Manufacturing of Wind Turbine Molds.* Oak Ridge, TN: Oak Ridge National Laboratory. NFE-16-06051. https://doi.org/10.2172/1376487.

Post, B. K., B. Richardson, R. Lind, L. J. Love, P. Lloyd, V. Kunc, B. J. Rhyne, et al. 2017b. "Big Area Additive Manufacturing Application in Wind Turbine Molds." Presented at the 28th Annual International Solid Freeform Fabrication Symposium, Austin, TX, August 7–9. https://www.osti.gov/biblio/1548257.

Shen, C.-H., and G. S. Springer. 1976. "Moisture Absorption and Desorption of Composite Materials." *Journal of Composite Materials* 10 (1): 2–20. https://doi.org/10.1177/002199837601000101.

Singh, R., S. Singh, I. P. Singh, F. Fabbrocino, and F. Fraternali. 2017. "Investigation for Surface Finish Improvement of FDM Parts by Vapor Smoothing Process." *Composites Part B: Engineering* 111: 228–234. https://doi.org/10.1016/j.compositesb.2016.11.062.

Türk, D.-A., A. Ebnöther, M. Zogg, and M. Meboldt. 2018. "Additive Manufacturing of Structural Cores and Washout Tooling for Autoclave Curing of Hybrid Composite Structures." *Journal of Manufacturing Science and Engineering* 140 (10): 105001. https://doi.org/10.1115/1.4040428.

Wang, Chen, Avantika Singh, Erik G. Rognerud, Robynne Murray, Grant M. Musgrave, Morgan Skala, Paul Murdy, et al. 2023. "Synthesis, Characterization, and Recycling of Bio-Derivable Polyester Covalently Adaptable Networks for Industrial Composite Applications." *Matter* 7 (2): 550–568. https://doi.org/10.1016/j.matt.2023.10.033.

WPTO. 2022a. *Summary Report: October 5, 2021 Workshop on Materials & Manufacturing for Marine Energy Technologies.* United States: Water Power Technologies Office. https://www.energy.gov/sites/default/files/2022-05/eere-materials-and-manufacturing-for-marine-energy-summary-report.pdf.

WPTO. 2022b. *Water Power Technologies Office: Multi-Year Program Plan.* United States: Water Power Technologies Office. https://www.energy.gov/sites/default/files/2022-03/wpto-mypp-2022-1.pdf.

Appendix. Specimen Failure Modes

Figure A-1 through Figure A-17 show failure images and micrographs of the specimens tested at Montana State University to correspond with the data presented in section 3.2.2.

Figure A-1. Photo of ASTM D638 tensile-tested Ultem 9085 series

Photo by Daniel Samborsky, MSU

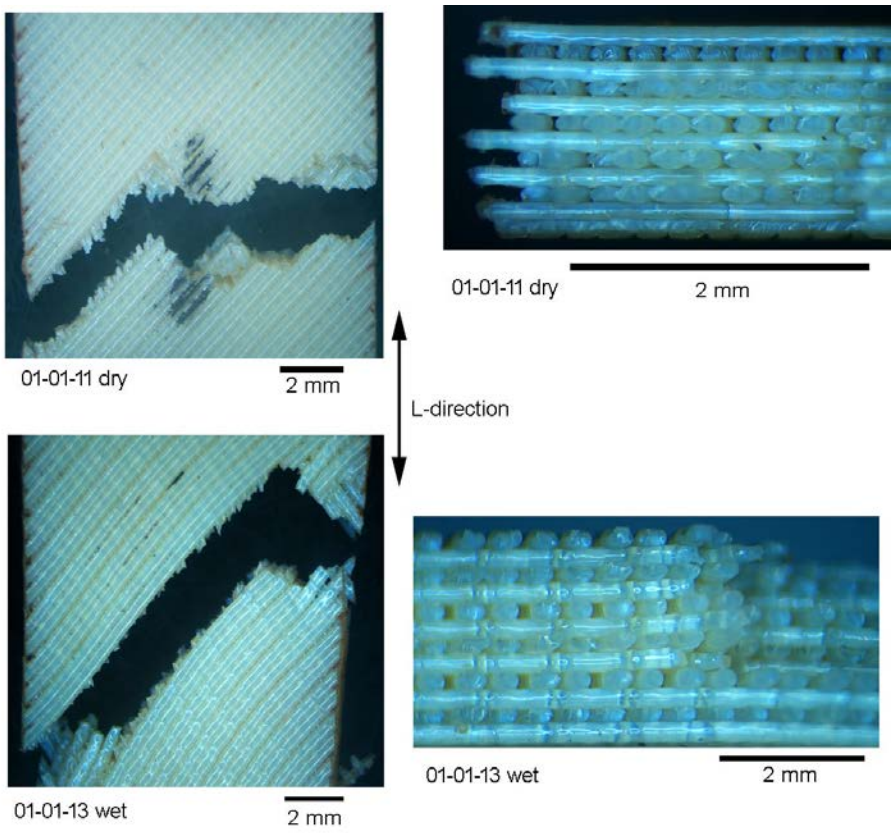

Figure A-2. Micrographs of the typical Ultem 9085 ASTM D638 tensile failure surfaces

Photos by Daniel Samborsky, MSU

Figure A-3. Photo of ASTM D638 tensile failures in the ASA specimens

Photo by Daniel Samborsky, MSU

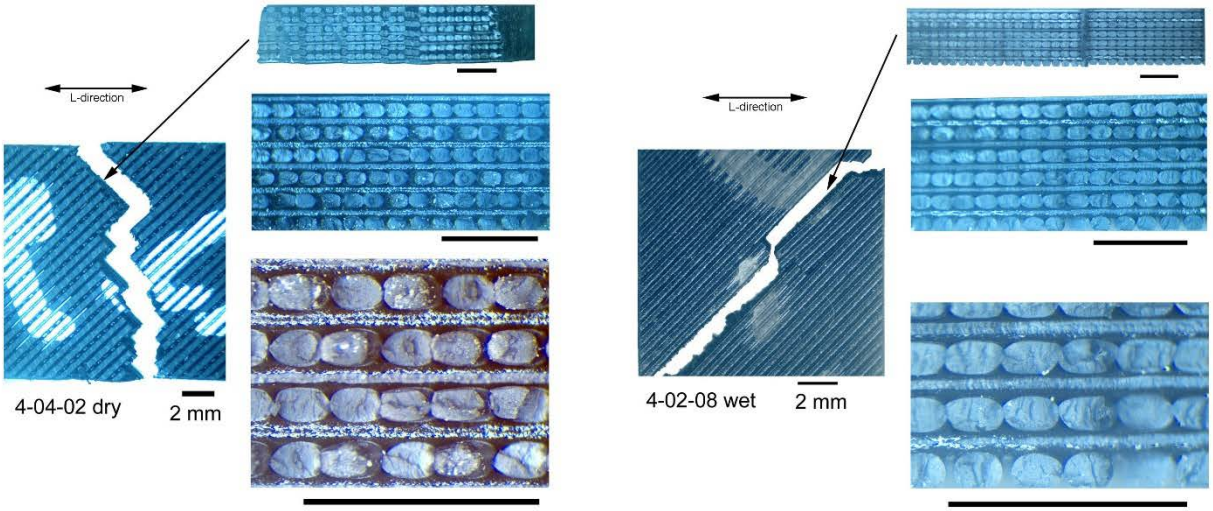

Figure A-4. Micrographs of the typical ASA tensile failure surfaces (all micrographs have an associated 2-mm scale bar)

Photos by Daniel Samborsky, MSU

Figure A-5. Photo of ASTM D638 tensile-tested Onyx material series

Photo by Daniel Samborsky, MSU

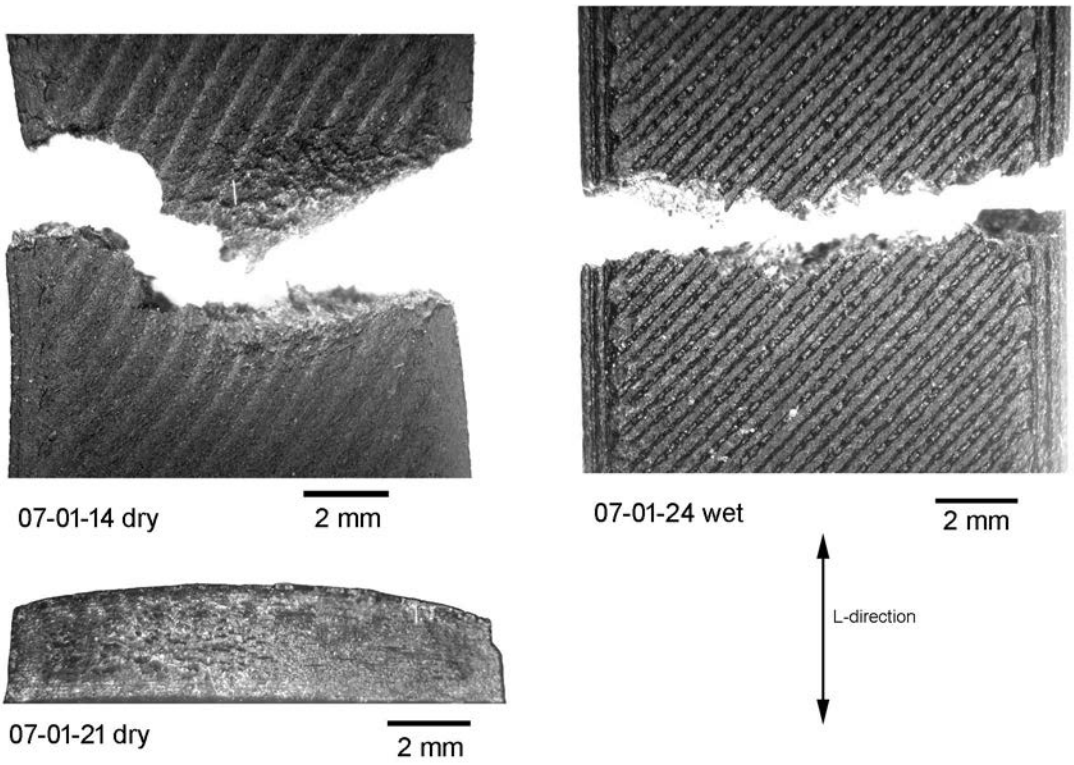

Figure A-6. Photo of the failure surfaces of the tensile-tested Onyx material series

Photo by Daniel Samborsky, MSU

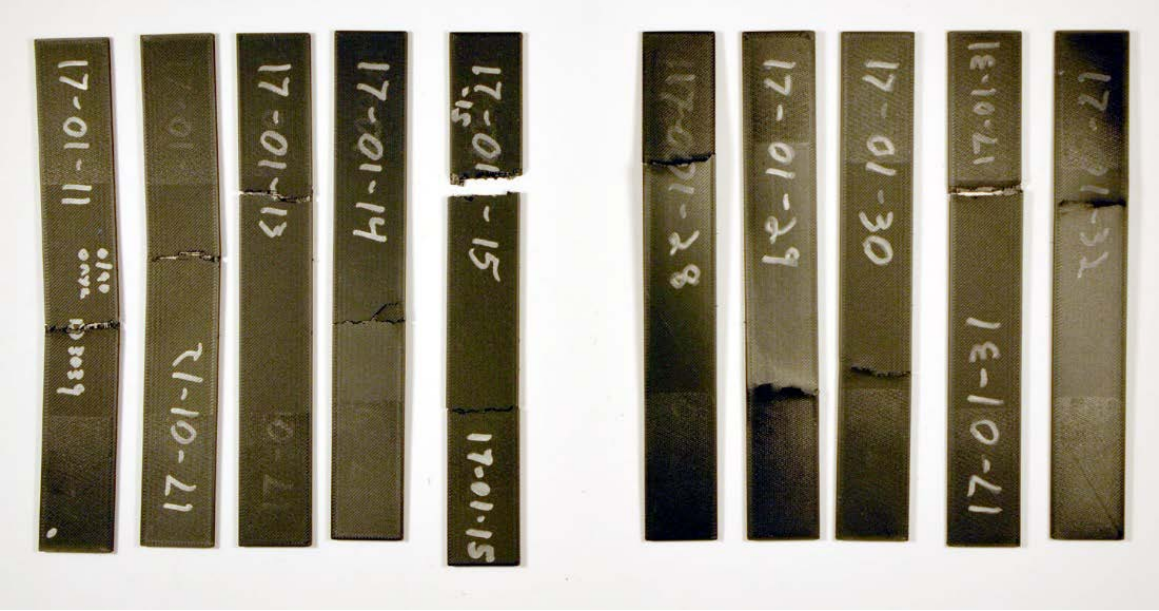

Figure A-7. Photo of ASTM D3039 tensile failure of the Onyx/carbon fiber series. Notably, liquid water was squeezed out of two of the test specimens while in the hydraulic wedge grips when clamped and tested.

Photo by Daniel Samborsky, MSU

Figure A-8. Photo of the ASTM D3039 tensile failures in the Onyx/glass fiber series

Photo by Daniel Samborsky, MSU

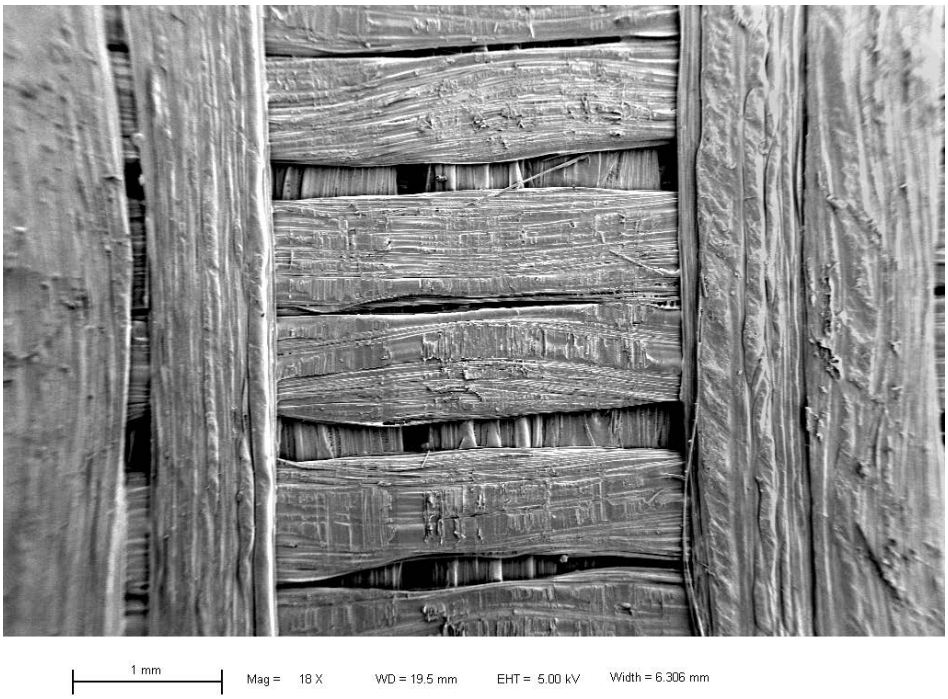

Figure A-9. Scanning electron micrograph of Onyx/glass fiber failure surface. The lack of fusion from filament to filament produced through-thickness pores.

Image by Daniel Samborsky, MSU

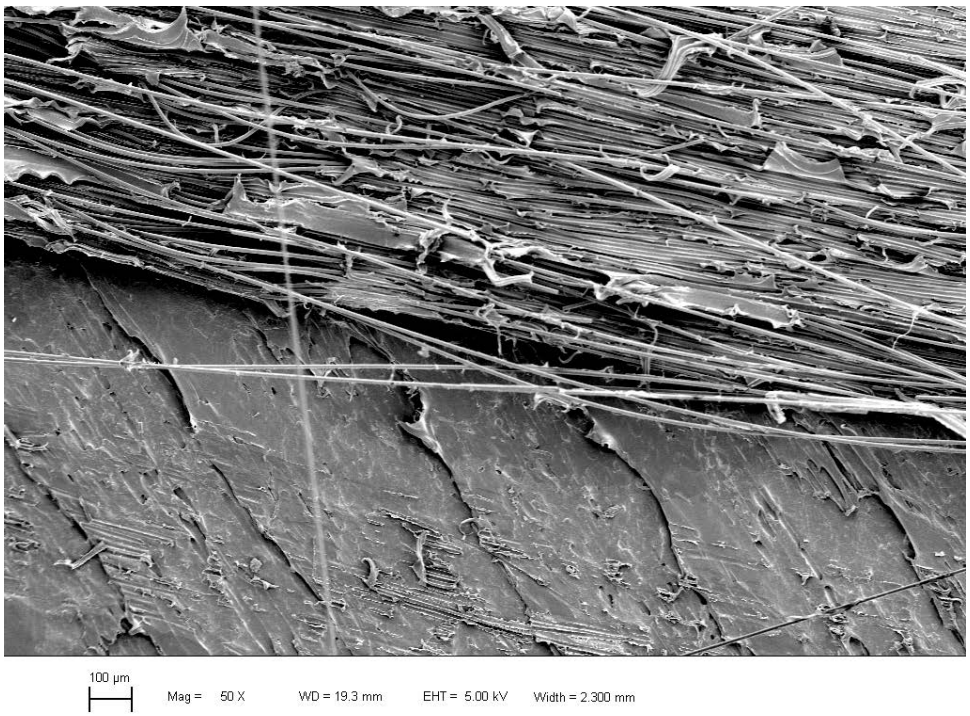

Figure A-10. Scanning electron micrograph of Onyx/glass fiber failure surface. Top fiber filament and underlying clean lower ply surface are present.

Image by Daniel Samborsky, MSU

Figure A-11. Scanning electron micrograph of Onyx/glass fiber tensile failure surface. Delamination surface shows clean underlying ply with little adhesion from the removed ply.

Image by Daniel Samborsky, MSU

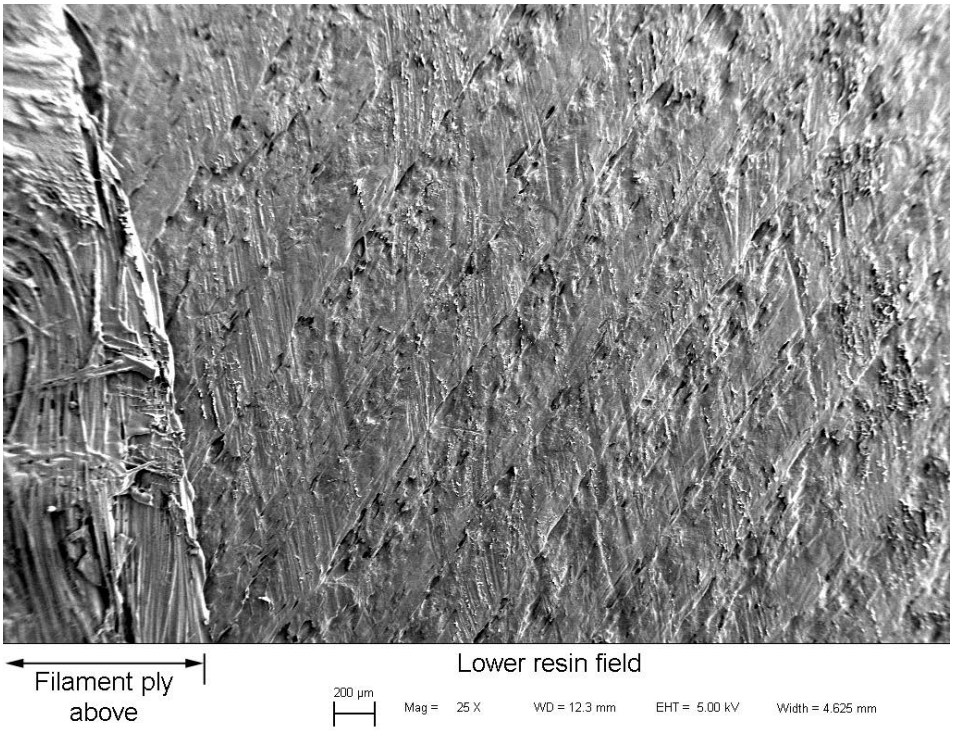

Figure A-12. Scanning electron micrograph of Onyx/carbon fiber tensile failure surface. Delamination surface shows clean underlying ply with little adhesion from the removed ply. A single filament is seen on the left-hand side of the micrograph.

Image by Daniel Samborsky, MSU

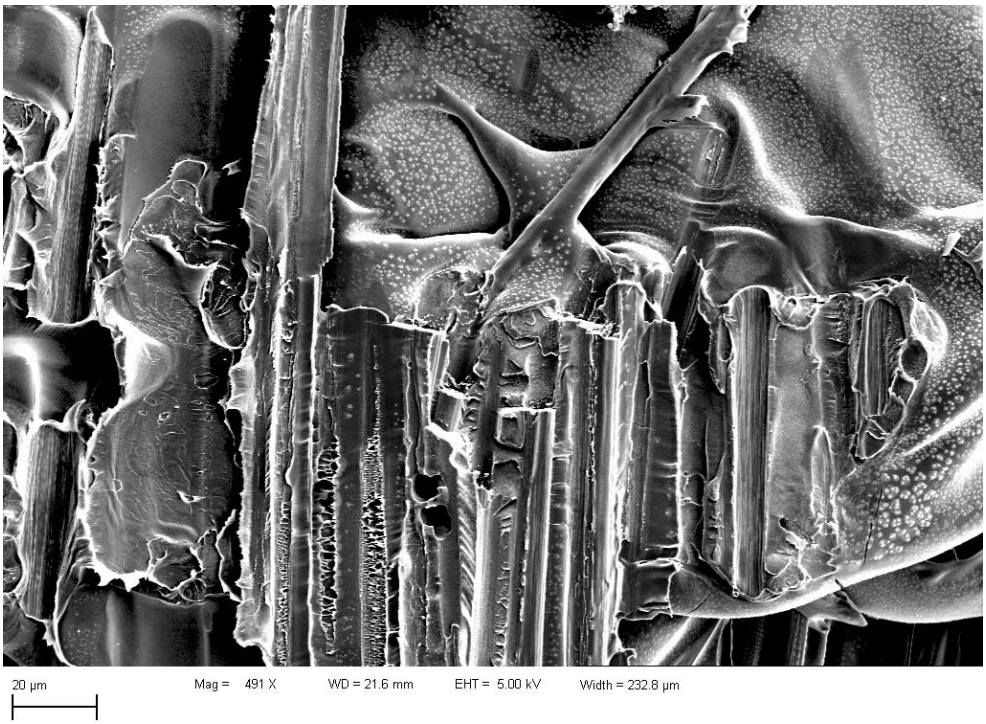

Figure A-13. Scanning electron micrograph of Onyx/carbon fiber tensile failure surface. Interior voids show the presence of a white film of dots. These white dots are present only on the Onyx/carbon fiber interior voids of the wet conditioned specimens. This film was not present on the dry failure.

Image by Daniel Samborsky, MSU

Figure A-14. Higher-magnification scanning electron micrograph of Onyx/carbon fiber tensile failure surface. Interior voids show the presence of a white film of dots.

Image by Daniel Samborsky, MSU

Figure A-15. Photo of the shear failures in the ASTM D7078 Ultem 9085 series

Photo by Daniel Samborsky, MSU

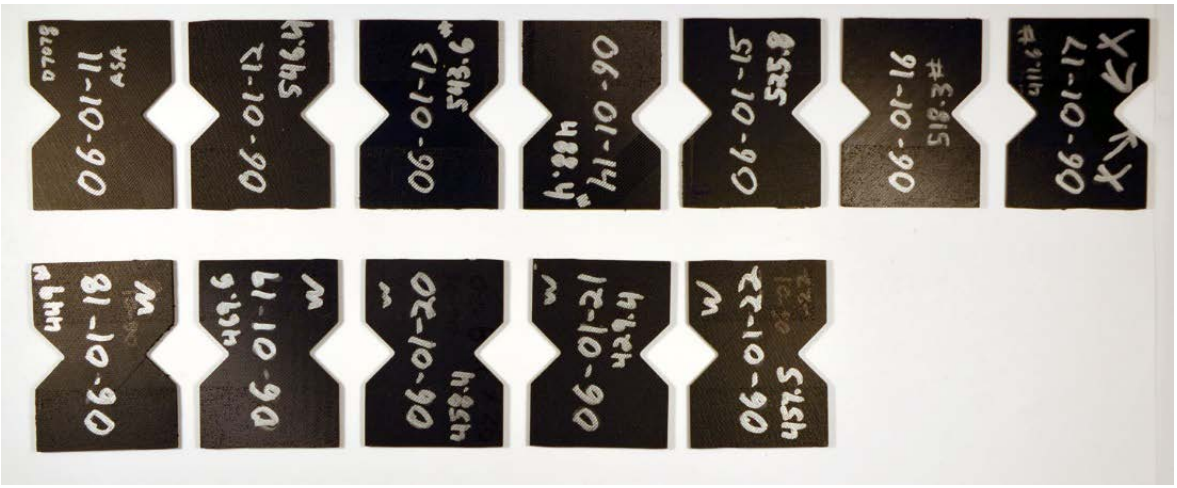

Figure A-16. Photo of the shear failures in the ASTM D7078 ASA series

Photo by Daniel Samborsky, MSU

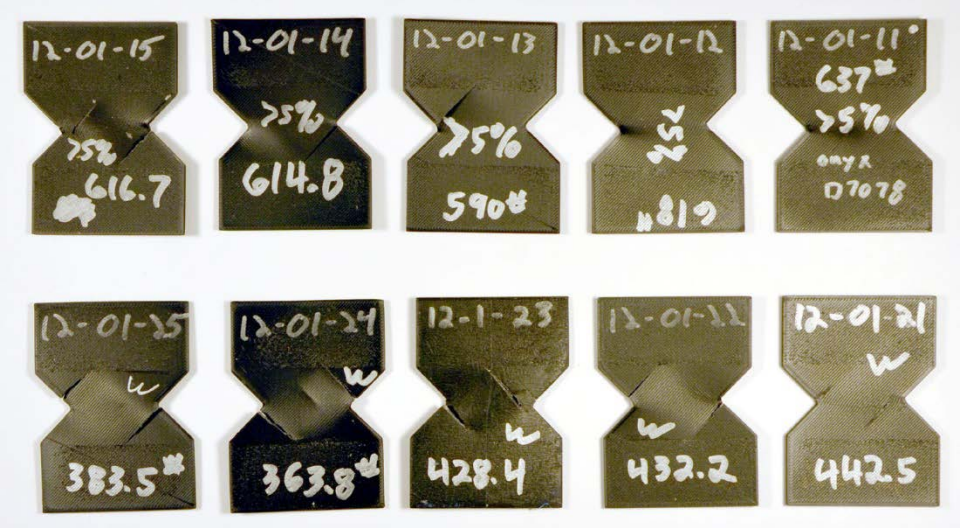

Figure A-17. Photo of the shear failures in the ASTM D7078 Onyx series. Out-of-plane deformation was large in this material; hence, strengths should be viewed with caution.

Photo by Daniel Samborsky, MSU